Acta Pharmaceutica Sinica B 2026;16(7):4083−4102

Chinese Pharmaceutical Association
Institute of Materia Medica, Chinese Academy of Medical Sciences

Acta Pharmaceutica Sinica B

www.elsevier.com/locate/apsb
www.sciencedirect.com

ORIGINAL ARTICLE

Engineering selective PI3Kγ inhibitors with antitumor and immunomodulatory potentials

Yi Zuo[a,b,†], Yiru Pu[a,†], Jianan Liu[a,c,†], Hongyu Chen[a,b,†], Yao Chen[a], Xinlan Li[a], Yan Wang[a], Tingting Zhang[a], Hongbin Cheng[d,*], Jin Liu[e], Yun Deng[a], Zhaotong Cong[b], Maolin Wang[c,f,*], Jun Lu[a,*], Shilin Chen[b,*]

[a]*State Key Laboratory of Southwestern Chinese Medicine Resources, School of Pharmacy, Chengdu University of Traditional Chinese Medicine, Chengdu 611137, China*
[b]*Institute of Herbgenomics, Innovative Institute of Chinese Medicine and Pharmacy, Chengdu University of Traditional Chinese Medicine, Chengdu 611137, China*
[c]*Clinical Research Center, The First Affiliated Hospital of Shantou University Medical College, Shantou 515041, China*
[d]*Department of Dermatology, Hospital of Chengdu University of Traditional Chinese Medicine, Chengdu 610075, China*
[e]*Institute for Advancing Translational Medicine in Bone & Joint Diseases, School of Chinese Medicine, Hong Kong Baptist University, Hong Kong SAR 999077, China*
[f]*Department of Physiology, School of Basic Medical Sciences, Shenzhen University, Shenzhen 518037, China*

Received 4 July 2025; received in revised form 2 September 2025; accepted 15 September 2025

KEY WORDS

PI3Kγ-targeted inhibitor;
Machine learning;
Molecular hybridization;
Indole-hybrid aromatic ring;
PI3K/AKT/NF-κB signaling axis;

Abstract PI3Kγ represents a promising therapeutic target for its pivotal role in macrophage recruitment and polarization and its significant association with tumor invasion and metastasis. In this study, a series of novel indole-based PI3Kγ selective inhibitors were generated by machine learning combined with molecular hybridization. Intriguingly, the representative **IHA-5f** displayed picomolar-level potency and highly selective inhibition to PI3Kγ relative to PI3Kα/β/δ. Moreover, **IHA-5f** manifested prominent anti-melanoma activity *in vitro* and *in vivo* with no detectable visceral toxicity. Mechanistically, **IHA-5f** efficiently suppressed tumor cell proliferation and migration, and induced apoptosis by suppressing the

This article is part of special issue entitled Machine Learning in Drug Discovery.

*Corresponding authors.
E-mail addresses: chenghongbin@cdutcm.edu.cn (Hongbin Cheng), wangml1240@163.com (Maolin Wang), ljaaa111@163.com (Jun Lu), slchen@cdutcm.edu.cn (Shilin Chen).
†These authors made equal contributions to this work.

Peer review under the responsibility of Chinese Pharmaceutical Association and Institute of Materia Medica, Chinese Academy of Medical Sciences.

https://doi.org/10.1016/j.apsb.2025.11.011

Tumor-associated macrophage reprograming;
Immunomodulation;
Melanoma treatment

PI3Kγ/AKT/NF-κB signaling axis. Concurrently, it restrained the M2 polarization of tumor-associated macrophages, thereby augmenting the antitumor immune response. This study underscores the potential for PI3Kγ inhibitors as immunomodulators and direct antitumor agents.

1. Introduction

Phosphatidylinositol 3-kinase gamma (PI3Kγ), the sole class IB isoform orchestrating immune microenvironment remodeling, has emerged as a groundbreaking immunotherapeutic target for solid tumors[1,2]. Distinct from other PI3K isoforms, PI3Kγ governs myeloid-derived suppressor cell infiltration and tumor-associated macrophage (TAM) polarization through G protein-coupled receptor (GPCR)-mediated signaling cascades, establishing an immunosuppressive niche that facilitates tumor immune evasion[3,4]. Recent clinical evidence highlights that selective PI3Kγ inhibition not only reprograms TAM-M2 polarization but also synergistically enhances checkpoint blockade efficacy in PD-L1 low malignancies, addressing a critical unmet need in contemporary immunotherapy[5-7]. Additionally, PI3Kγ suppression mitigates the resistance of tumor cells to immunotherapies such as *PD-1* and *CTLA-4* antibodies[8,9]. These findings position PI3Kγ as a master regulator bridging innate and adaptive antitumor immunity.

The early development of PI3K-targeted agents primarily focused on pan-PI3K inhibitors[10,11]. However, these agents exhibit a lack of selectivity, resulting in significant adverse effects, including diarrhea, anemia, thrombocytopenia, and hyperglycemia[12,13]. Consequently, there is an urgent need to develop PI3K isoform-specific inhibitors. Notably, PI3Kγ has garnered considerable interest as a potential immunotherapeutic target[14]. The pharmaceutical design of PI3K inhibitors is mainly based on the ATP-binding pocket, which is partitioned into four main structural regions, including the hinge region, the specificity pocket, the hydrophobic region I, and the hydrophobic region II. Typically, PI3K inhibitors are anchored to the backbone chain in the hinge region *via* hydrogen bonding[15,16]. Within the 14 amino acids proximal to the hinge region, only Lys883γ, Asp884γ, Thr886γ, and Lys890γ are completely distinct across the four isoforms, while the remaining residues are highly conserved[17,18]. Considering the sequence homology of the class I PI3K active sites and the tightly conservative topology of the ATP-binding loci with intimately related protein kinases (*e.g.*, mTOR and DNA-PK), the development of PI3Kγ-specific inhibitors presents a formidable challenge[19,20]. Currently, only eganelisib has reached the clinical study stage as a PI3Kγ-specific inhibitor for the treatment of advanced head and neck cancer, breast cancer, etc[21].

In recent years, the rapid advancement of computer-aided drug design (CADD) has revolutionized drug discovery, offering unparalleled capabilities for analyzing complex datasets and accurately predicting molecular properties[22-24]. Additionally, water molecules play a pivotal role in drug design, stabilizing drug-target interactions and enhancing the selectivity through hydrogen bonding and other interactions. This study employed advanced machine learning algorithms combined with a large-scale compound database to identify molecules that specifically inhibit PI3Kγ. Utilizing CADD software and water molecule-guided strategies, we conducted thorough fragment analysis, pharmacophore identification, and structural optimization, resulting in the synthesis of a series of high-activity, selective PI3Kγ inhibitors featuring unique indole-hybrid aromatic ring (IHA) structures. These compounds selectively target PI3Kγ by binding to specific residues on PI3K subtypes[25,26]. Notably, the representative **5f** demonstrated exceptional PI3K inhibitory activity, with an IC_{50} value as low as 0.11 nmol/L. IHAs suppressed tumor cell proliferation and facilitated apoptosis through the PI3K/AKT/NF-κB signaling axis, and selectively inactivated PI3Kγ in TAM to activate the NF-κB, thereby inhibiting the M2 polarization and exerting anti-tumor effects. This study provides critical insights for developing next-generation kinase inhibitors with enhanced specificity, offering a novel therapeutic strategy to simultaneously disrupt tumor cell intrinsic signaling and reshape the immunosuppressive microenvironment.

2. Materials and methods

2.1. Chemistry

All the starting materials were obtained from Shanghai Macklin Biochemical Co., Ltd. (Shanghai, China) and Chengdu Pukang Biological Technology Co., Ltd. (Chengdu, China), and used without further purification unless otherwise stated. Reactions were monitored by thin-layer chromatography (TLC) using precoated silica gel plates (silica gel GF/UV 254), and spots were visualized under UV light (254 nm). The flash column chromatography was performed *via* silica gel (200−300 mesh). Accurate mass measurements were performed on the electrospray ionization (ESI) apparatus using an Agilent 1260-Bruker tims TOF mass (MA, USA). ^{1}H NMR and ^{13}C NMR spectra were recorded on a Bruker-600 MHz spectrometer or a Bruker-700 MHz spectrometer (Bremen, German). Chemical shifts (δ) were given in parts per million (ppm), and the residual solvent peaks were used as an internal reference ($CDCl_3$: δ 7.26 ppm ^{1}H; δ 77.2 ppm ^{13}C; MeOD-d_4: δ 3.31 ppm ^{1}H; δ 49 ppm ^{13}C; DMSO-d_6: δ 2.50 ppm ^{1}H; δ 39.5 ppm ^{13}C). Coupling constants (J values) were reported in hertz. Splitting patterns were designated as follows: s, singlet; d, doublet; t, triplet; q, quartet; m, multiples. The purity of all the final compounds was measured by HPLC (Shimadzu LC-16, Kyoto, Japan) analysis and confirmed to be >95% (75%−95% ACN in H_2O containing 0.1% formic acid, 0.8 mL/min flow rate) with a C18 column (SWELL Chromplus C18 5 μm, 4.6 mm × 250 mm).

2.2. Biology

PI3Kγ inhibitor IPI-549, PI3K activator 740 Y-P, 5-FU, and dacarbazine were obtained from Macklin (Shanghai, China).

RPMI 1640 and DMEM medium were purchased from Corning (New York, USA). 3-(4,5-Dimethylthiazol-2-yl)-2,5-diphenyl tetrazolium bromide methyl thiazolyl tetrazolium (MTT), sodium dodecyl sulfate (SDS), dimethyl sulfoxide (DMSO), glycine, tris, and trypsin were obtained from Biofroxx. Fetal bovine serum (FBS) was supplied by ExCell Bio (Shanghai, China). Penicillin-streptomycin and trypsin were provided by Biofrox (Cambridge, UK). Nitric Oxide Assay Kit with DAF-FM DA, Annexin V-FITC Apoptosis Assay Kit, Reactive Oxygen Species Assay Kit, BCA kit, EdU Assay Kit, and Cell Cycle and Apoptosis Analysis Kit were provided by Beyotime (Shanghai, China). ADP-Glo™ lipid kinase system was purchased from Promega (Shanghai, China). IL-4, IL-13, and LPS were purchased from Chamot Biotechnology (Shanghai, China). IL-1β, IL-6, and TNF-α ELISA Kits were purchased from Beijing 4A Biotech (Beijing, China). The following antibodies were obtained from Biolegend (San Diego, CA, USA): PE-anti-mouse CD86, APC-anti-mouse CD11b, FITC-anti-mouse F4/80. PE/Cy7-CD11b, V450-CD45, and Fixable Viability Stain (FVS) 780 were purchased from BD Bioscience (San Jose, CA, USA). Antibodies against CASPASE 3/8/9, cleaved CASPASE 3/8/9, BAX, BCL-2, PI3Kγ, p-PI3Kγ, AKT, p-AKT, and PARP were bought from Cell Signaling Technology (Danvers, MA, USA). Antibodies against β-Actin, β-Tubulin, CYT C, IKK, p-IKK, IKB, p-IKB, P65, p-P65, CYCLIN A, and CDK 2 were obtained from Wanleibio (Shenyang, China). CD206, ARG 1, and CD86 monoclonal antibodies were obtained from Abcam (Cambridge, MA, USA). Horseradish peroxidase (HRP) conjugated AffiniPure goat anti-rabbit/mouse IgG (H + L) (BA1056) was obtained from BOSTER (Wuhan, China).

2.3. Bioinformatics analysis

Clinical information and corresponding RNA-seq data of cancer were obtained from the TCGA database (https://portal.gdc.cancer.gov/). The raw data were normalized using the fragment per kilobase of exon per million fragments mapped (FPKM) method, and log2 (FPKM+1) transformation was applied for the subsequent analyses. The infiltration levels of TAMs (M1 and M2) in TCGA cancer patients were evaluated by CIBERSORT, CIBERSORT-ABS, and XCELL. Scores were directly downloaded from the TIMER 2.0 database (http://timer.cistrome.org/). The gene expression profile datasets (GSE58318) deposited in the GEO (http://www.ncbi.nlm.nih.gov/geo/) database were used to investigate the differential expression of P110$\gamma^{-/-}$ and WT mice in peritoneal macrophages. Differential genetic analysis was performed using the GEO online analytical tool easyGEO (https://tau.cmmt.ubc.ca/eVITTA/easyGEO/).

2.4. Compound database analysis

The inhibitor structures of the four PI3K subunits were retrieved from the commercial database GOSTAR. A custom query was formulated within the querying interface of GOSTAR, targeting molecules identified as inhibitors of the PI3K subunits. The search criteria encompassed chemical structure identifiers and known activity data against PI3K.

The cheminformatics tool RDKit was employed to guarantee high-quality data. Any duplicate entries were identified and eliminated. Each chemical structure was verified for its completeness and correctness. Structures with inconsistent bond formation or missing atoms were excluded from the dataset. Inhibitors were cross-referenced with activity data to confirm their interaction with at least one subunit of PI3K.

2.5. Molecular fingerprinting

ECFP (Extended Connectivity Fingerprint) is a type of circular fingerprint. In ECFP4, the generation process includes mapping the atoms in the molecule to a series of unique identifiers through an iterative hashing process. We used the GetMorganFingerprintAsBitVect method from the RDKit library to generate the ECFP4 descriptor.

2.6. Algorithms

Naive Bayes (Bay), Random Forest (RF), Support Vector Machine (SVM), Fingerprints and Graph Neural Networks (FP-GNN), and Neural Network (NN) algorithms were employed to construct the classification models. The libraries DeepChem and scikit-learn were imported for the implementation of each machine-learning method. All hyperparameters used for the Bay, NN, SVM, RF, and FP-GNN models have been documented and made publicly available. Detailed information could be found in the code repository at the following link: https://github.com/MaolinWang/pi3k_ML_hyperpara.

2.7. Computer-aided molecular design

The Brood software (OpenEye Scientific, Santa Fe, NM, USA) was utilized with its default settings to generate novel molecular structures by systematically replacing fragments to explore a diverse chemical space and identify potential modifications. The fragment database ChEMBL31 encompassed all possible fragments with medicinal significance. The Druglike preset filter properties were set within the following ranges: Synthetic Accessibility $\geq$1, Molecular Weight $\leq$1000, Rotor Count $\leq$10, Log$P$ $\leq$5.0, Lipinski Donor Count $\leq$5, Lipinski Acceptor Count $\leq$10, and Lipinski Failures $\leq$1.

ROCS from OpenEye Scientific Software was utilized for pharmacophore identification. ROCS operates on the principle that molecules with similar shapes often exhibit similar biological activities, making it a powerful tool for virtual screening, scaffold hopping, and lead optimization. It is widely used in computational chemistry and drug discovery to compare molecular shapes and identify compounds with similar 3D structures.

2.8. Hydration site analysis

SZMAP from OpenEye Scientific Software assessed the manner and locations where water interacts with specific sites on a molecule, providing insights into hydrophobicity, affinity, and potential energetic interactions. SZMAP produced a diagram that reflected changes in thermodynamic characteristics. Regions exhibiting minimal energy fluctuations implied advantageous interactions and probable hydrophilic locations.

2.9. Molecular docking

The docking process involves the prediction of the binding direction and affinity between small molecules (ligands) and target

proteins, which is essential in drug design and discovery. The three-dimensional (3D) structure of the target protein was obtained from the Protein Data Bank (PI3Kα ID: 7k6n, PI3Kβ ID: 4AJW, PI3Kδ ID: 6TNR, PI3Kγ ID: 6C1S). Before docking, the protein structure requires preprocessing steps such as removing water molecules, co-factors, energy minimization, and optimization techniques to relax the structure and remove steric clashes. Small molecules (ligands) also need to be prepared to generate appropriate 3D structures by using OMEGA software from OpenEye Company. Then FRED from OpenEye Corporation was employed as an exhaustive docking algorithm to explore in depth the conformational space of the ligand and the protein receptor.

2.10. Molecular dynamics simulations

Molecular dynamics (MD) simulations were performed using GROMACS version [2024.04] (Gromacs, Groningen, Netherlands)[27]. The system was prepared using the Amber99SB force field, which is well-suited for simulating biomolecular systems. The initial structure of the protein-ligand (PI3Ks-**5f**) complex was obtained from docking results. The complex was solvated in a cubic box of TIP3P water molecules, with a minimum distance of 1.0 nm from the protein surface to the box edge. Sodium and chloride ions were added to neutralize the system.

Energy minimization was conducted using the steepest descent algorithm for 5000 steps, followed by a conjugate gradient minimization for an additional 5000 steps to ensure the system was in a stable conformation. The system was then equilibrated in two phases: first, the NVT ensemble was simulated for 100 ps at 300 K, followed by the NPT ensemble for 100 ps at 1 atm pressure. The production MD run was carried out for 10 ns under NPT conditions, with a time step of 2 fs. The temperature and pressure were maintained using the V-rescale and Parrinello-Rahman methods, respectively.

2.11. MMPBSA binding energy calculation

The binding free energy of the protein−ligand complexes was calculated using the MMPBSA method implemented in GROMACS through the gmx_MMPBSA tool[28]. The trajectory files from the MD simulations were analyzed to extract the relevant frames for binding energy calculations. The polar solvation energy was calculated using the MMGBSA method. The calculations were performed over 300 frames extracted from the 10 ns of the MD trajectory to ensure statistical relevance.

2.12. PI3K isoform ADP-Glo assay

The PI3K-GLO™ Class I Rapid Kinase Detection Kit was utilized to determine the inhibitory activity of inhibitors on PI3K isoforms. According to the instructions provided by the reagent manufacturer, equal volumes of PI3K Reaction Buffer and Lipid Substrate were mixed, diluted with the corresponding kinases, and incubated in each well for 20 min at room temperature. The reaction was initiated by adding ATP to each well and incubated continuously at 25 °C for 1 h. Then, ADP-Glo reagent was added to each well to stop the enzyme reaction and deplete the unconsumed ATP. Finally, the kinase detection reagent was added to each well to convert ADP to ATP, and luciferase and luciferin were introduced to detect ATP. After a fluorescent signal was generated, the 384-well plate was measured using an Envision microplate reader (Molecular Devices, MD SpectraMax iD5, Shanghai, China).

2.13. QSAR analysis

PyMoLSAR (Schrödinger, LLC, New York, NY, USA) was employed for structure-based QSAR analysis. All synthesized compounds were randomly divided into training and testing sets, with **5d**, **7f**, **8j**, **8r**, **10b**, and **11d** serving as the testing set and the remaining compounds forming the training set. The activity field was expressed as the negative logarithm of PI3Kγ cell activity (*i.e.*, pIC_{50} value), and five molecular descriptors were selected for modelling analysis. A database containing experimental results and molecular structural information was established. By adopting the PLS model, the experimentally measured biological activity was correlated with selected molecular descriptors, and the expected activity of the compounds in the test set was predicted accordingly.

2.14. Cell lines and culture

B16, MCF-7, HCT116, LO2, and HEK293 cell lines were purchased from the Cell Bank of Type Culture Collection of the Chinese Academy of Sciences, China (Shanghai, China). Cells were cultured in DMEM or 1640 medium at 37 °C in a humidified incubator containing 5% CO_2, and all media were supplemented with 10% FBS and 1% penicillin−streptomycin.

2.15. MTT assay

Cells in the logarithmic growth phase were inoculated into the 96-well plate at an appropriate concentration. After the cells had been attached, various concentrations of compounds were added to them in triplicate for a 48 h incubation period. Then cells were incubated with 20 μL MTT (5 mg/mL) for 2 h at 37 °C, and the medium was replaced with 100 mL DMSO. The plates passed through a microplate reader were determined at 490 nm wavelength (Molecular Devices).

2.16. Colony-formation assay

B16 and A375 cells were seeded into 6-well plates with a density of 500 cells/well and treated with **5f** in different concentrations. After incubation for 24 h, the medium without serum was used to replace the serum-containing medium. The cells were fixed with 4% paraformaldehyde after 14 days of culture, stained with 0.1% crystal violet, washed in the background with PBS, and then observed under the microscope and counted the number of colonies. Clones containing >50 cells were counted under an inverted microscope (Phenixoptics, XDS200, Jiangxi, China).

2.17. EdU assay

B16 and A375 cells were seeded on sterile glass coverslips at appropriate concentrations and treated with **5f** in different concentrations for 24 h. Then cells were treated with 10 μmol/L EdU for 1 h, fixed, and underwent Click-iT chemistry to stain. After labeling, the cell nuclei were stained with DAPI, and the samples were visualized by a laser-scanning confocal microscope (Leica

Biosystems, Leica DM6B, Deer Park, IL, USA). Three random views were used to calculate the average EdU/DAPI ratio (× 100%).

2.18. Cell-cycle analysis

B16 and A375 cells were inoculated in 6-well plates (4×10^4 cells/well), and treated with the indicated concentrations of **5f** for 48 h. Cells were collected by digestion, washed twice with PBS, and then fixed overnight in pre-cooled 70% ethanol at 4 °C. Then, cell cycles were analyzed using propidium iodide (PI) staining, and fluorescence was measured by a flow cytometer (BD Biosciences, BD FACSVerse, NJ, USA). Cell cycle profiles were analyzed by ModFit Cell Cycle Analysis software (Topsham, Verity Software House, ME, USA).

2.19. Western blot analysis

Cells treated with different concentrations of **5f**, IPI-549 (10 μmol/L), 740 Y-P (2 μmol/L), LPS (100 μg/L), and IL-4/IL-13 (20 μg/L) alone or in combinations for 24 h were washed with cold PBS and collected by RIPA-containing cocktail and PMSF on ice. The suspension was centrifuged at 13,000 rpm at 4 °C for 15 min (UCHEN, LC-LX-HR165A, Shanghai, China). Protein concentrations were measured using a BCA Protein Assay Kit. Protein samples were separated by 12.5% SDS-PAGE or 10% SDS-PAGE and then transferred to PVDF membranes. The membranes were blocked with 5% nonfat dry milk for 2 h at room temperature and then incubated with primary antibodies (1:1000 dilution) at 4 °C overnight. Then, the membranes were washed three times with TBS-T buffer and incubated with appropriate HRP-conjugated secondary antibodies at room temperature for 1 h. Finally, the protein bands were detected with enhanced chemiluminescence (ECL) Kit, and the results of each band were quantified by ImageJ software (Madison, ImageJ, WI, USA).

2.20. CETSA assay

Cells treated with the indicated concentrations of **5f** for 2 h were collected with PBS containing protease inhibitors and transferred to 200 μL EP tubes. Then cells were heat shocked at 45−61 °C for 3 min and cyclically lysed in liquid nitrogen to 25 °C 3 times, followed by centrifugation at 4 °C, 12,000 rpm for 20 min (UCHEN). Finally, a loading buffer was added for standard Western blot operation (Hercules, Bio-Rad Laboratories, CA, USA).

2.21. Apoptosis assay

B16 and A375 cells were individually seeded into 6-well plates and treated with **5f** at different concentrations for 48 h after cell adherence. Then cells were digested and collected with trypsin, centrifuged, and washed. Then 5 μL FITC-Annexin V and 10 μL PI working solution were added to each group at 25 °C for 10 min in the dark. After staining, the samples were analyzed by flow cytometry (BD Biosciences).

2.22. Reactive oxygen species (ROS) assay

B16 and A375 cells were treated with **5f** at different concentrations for 12 h after cell adherence. Then cells were incubated with a serum-free medium containing DCFH-DA solution (10 μmol/L) at 37 °C for 30 min in the dark, washed twice with ice-cold PBS, and harvested in cold PBS. The final results were detected by flow cytometry (BD Biosciences).

2.23. Transwell migration assay

B16 and A375 cells were resuspended in 300 μL serum-free medium containing different concentrations of **5f** and seeded into the upper chamber of a Transwell, then 650 μL medium with 10% FBS was placed in the lower chamber. After incubating at 37 °C for 24 h, cells on the upper membrane surface were scraped off. The invasive cells were fixed with 4% paraformaldehyde, stained with 0.1% crystal violet, washed with PBS, and then dried. The results were observed under an inverted microscope (Phenixoptics).

2.24. Wound-healing assay

B16 and A375 cells were seeded into 6-well plates and cultured until approximately 90% confluence in monolayer cultures. Artificial scratches were created by the end of a 200 μL pipette tip and the cell debris was washed with PBS. After incubating in serum-free DMEM with the indicated concentration of **5f** for 24 h, cell migration was observed at 0 and 24 h post-induction of injury under a phase-contrast microscope (Phenixoptics). ImageJ (Madison) was employed to quantitatively measure the wound healing area.

2.25. Macrophage polarization

Raw 264.7 cells were inoculated in 6-well plates (2×10^5 cells/well). M1 macrophages were generated by treating Raw 264.7 cells with LPS (100 μg/L), whereas 20 μg IL-4 and 20 μg IL-13-treated Raw 264.7 cells were polarized to M2 macrophages for 48 h. Additionally, to investigate the effect of **5f** on macrophage polarization, Raw 264.7 cells were treated with **5f** and LPS alone or in combinations for 24 h. Thereafter, cells were harvested and centrifuged for flow cytometry assay (see below) (BD Biosciences).

2.26. Cell co-culture

A transwell chamber with a 0.4 μm pore diameter was applied to establish a co-cultivation system. Determining the effect of **5f** on TAMs polarization, Raw 264.7 cells (2×10^5 cells) were seeded in the lower chamber and treated with **5f** in different concentrations, and B16 cells were seeded (3×10^4 cells) in the upper layer. Then, the co-culture model was maintained at 37 °C, and the medium was substituted after incubation for 24 h. After incubating for 48 h, cells in the lower chamber were collected for further analysis. In addition, to investigate the effect of TAM-M2 after **5f** treatment on B16 cell activity. Raw 264.7 cells were seeded in the upper layer and treated with 20 ng/mL IL-4 and 20 ng/mL IL-13 with or without **5f** for 48 h. After that, Raw 264.7 cells were cultured in a new medium. Then, B16 cells were seeded in the lower chamber, and the co-culture model was maintained at 37 °C for 48 h. B16 cells were collected for further analysis.

2.27. Flow cytometry assay

The expression of the CD86 and the CD206 in macrophages was performed by flow cytometry using fluorochrome-conjugated

monoclonal antibodies. The TAMs were collected and washed with PBS. Fc receptors were blocked by incubation of the cells with purified anti-mouse CD16/CD32 for 15 min on ice. Afterward, the cells were stained with FITC-conjugated anti-mouse CD86 and PE-conjugated anti-mouse F4/80 for 30 min on ice. Cells were then washed with PBS and fixed in 4% paraformaldehyde for 15 min. Then the cell membrane was broken with 1% Triton X-100 at room temperature for 10 min and washed with PBS. Cells were stained with Cy5.5-conjugated anti-mouse CD206 for 30 min at room temperature. The TAMs were examined with a flow cytometer (BD Biosciences) and analyzed using the Flow Jo software (Ashland, Flow Jo V1, OR, USA).

2.28. Cytokine analysis

The treated TAM-M2 cells were seeded in 6-well plates and maintained for 48 h with and without **5f**. Then, the cell supernatant was harvested and centrifuged at 1500 g for 10 min at 4 °C to recollect the supernatant (UCHEN). The concentrations of TNF-α, IL-6, and IL-1β in the cell supernatant were gauged using enzyme-linked immunosorbent assay (ELISA) kits according to the manufacturer's instructions.

2.29. In vivo experiment

Male C57 mice (6−8 weeks old; 20−22 g) were supplied by Beijing SiPeiFu Biotechnology Co., Ltd. (Beijing, China). All animal procedures have been approved by the Experimental Animals Administrative Committee of Chengdu University of Traditional Chinese Medicine and were performed according to the relevant animal regulations (Registration number: TCM-2016−312, Chengdu, China). 2×10^6 B16 cells were subcutaneously inoculated into the axilla of C57 mice. When the tumor volume grew to about 70 mm^3, mice were randomly divided into five groups ($n = 6$) and treated with PBS, Dacarbazine (100 mg/kg), IPI-549 (10 mg/kg), **5f** (10 mg/kg, 20 mg/kg) through intraperitoneal injection. Tumor volumes and body weights of mice were measured and recorded every other day. After the *in vivo* anti-tumor experiment was completed, all mice were euthanized, and the tumor volume, weight, and organ weight were determined. A 4% paraformaldehyde solution was used to treat the organ. Tumors were used for cell extraction and histology analysis.

In the toxicity verification experiment, mice were divided into four groups ($n = 6$): PBS, **5f** (100 mg/kg, 150 mg/kg, 200 mg/kg). **5f** was administered intraperitoneally to mice daily until their body weight showed a downward trend. During the experiment, their general condition was observed daily, and their body weight changes were measured. Following this time point, blood samples were collected for liver and kidney function detection, and the H&E staining of major organs was also investigated.

2.30. Immunohistochemistry (IHC)

After incubation in 3% hydrogen peroxide and blocked serum, the sections were reacted with anti-KI67, anti-p-PI3K, and anti-p-IKB overnight, then incubated with a secondary antibody and washed with PBS. Sections were stained with a complex containing avidin and biotinylated HRP, then stained with DAB, and finally, the sections were counterstained with hematoxylin were examined under confocal microscopy (Olympus, Olympus FV-OSR, Guangzhou, China).

2.31. TUNEL assay

Tumor tissues were fixed and embedded in paraffin. Tissue sections were cut, deparaffinized, repaired, and permeabilized with protease K. Then, sections were stained with the Fluorescein (FITC) TUNEL Cell Apoptosis Detection Kit. The nuclei were stained with DAPI. Tumor sections were visualized under fluorescence microscopy (Olympus).

2.32. Pharmacokinetic study

5f was administered to C57 mice *via* intraperitoneal injection for pharmacokinetic studies. Blood samples (50 μL) were collected by retro-orbital venous at different time points (0.125, 0.25, 0.5, 1, 2, 4, 6, 8, 12, and 24 h). Heparinized blood was centrifuged for 10 min at 3500 rpm and 4 °C to obtain plasma (UCHEN). Subsequently, 25 μL of supernatant was aspirated and 5 times the volume of acetonitrile was added to precipitate proteins, followed by centrifugation at 14,000 rpm for 10 min (UCHEN). Next, the supernatant was transferred to another test tube and gently dried with nitrogen gas at 30 °C. The dried residue was redissolved in 30 μL of methanol, vortexed, and centrifuged at 10,000 × *g* for 5 min, then filtered through a 0.22 μm filter membrane[29]. An aliquot of 5 μL of supernatant was used for HPLC analysis (HPLC LC-40, Shimadzu Corporation, Kyoto, Japan). The pharmacokinetic properties of **5f** were performed using the DAS2.0 software (Mathematical Pharmacology Professional Committee of China, Shanghai, China).

2.33. Statistical analysis

Continuous data are presented as mean ± standard deviation (SD) in figures. The difference between two groups was analyzed using Student's *t*-test (for normally distributed data with equal variances). Multiple comparisons were performed using one-way analysis of variance (ANOVA) followed by Tukey's *post hoc* test. The P value < 0.05 was considered statistically significant. All statistical analyses were conducted using GraphPad Prism version 9.0 (GraphPad Software, La Jolla, CA, USA).

3. Results

3.1. PI3Kγ involvement in macrophage-mediated tumor immunosuppressive response

TAMs, infiltrating macrophages around tumor cells, are crucial immune cells in the tumor microenvironment and intimately associated with the modulation of tumor immune function. To accurately assess the composition of TAMs in the tumor microenvironment, immune infiltration analyses were performed for all cancers in the TCGA database with CIBERSORT, CIBERSORT-ABS, and XCELL, and the scores revealed that the infiltration level of TAM-M2 was substantially greater than that of TAM-M1 in cancers (Fig. 1A). In a survival analysis based on TAM (M1 and M2) profile-related genes and cancers, the expression levels of all TAM-M2 and TAM-M1 signature genes were negatively correlated and positively correlated with the prognosis of cancer patients, respectively (Fig. 1B and C, and Supporting Information

Fig. S1A and S1B). Subsequently, correlation analysis revealed a dense relevance between these TAM factors and PI3Kγ expression (Fig. 1D and E, and Fig. S1C and S1D). To further confirm whether PI3Kγ could regulate the expression of macrophage polarization-associated factors, the mRNA and protein expression of macrophages in the peritoneum of treated mice were analyzed as described in the GEO database. In p110$\gamma^{-/-}$ processed macrophages, the genes associated with immune activation, antigen presentation, and T cell activation were upregulated, whereas genes associated with immunosuppression and chemoattraction were repressed (Fig. 1F and G). Moreover, the analysis revealed that the expression levels of TAM-M2-related proteins, such as *Il10*, *Arg1*, and TAM-M1-related proteins such as *Il6*, *Il12b*, *Tnf*, and *Il1b* presented a downward and upward trend, respectively (Fig. 1H). Altogether, PI3Kγ could regulate macrophage switching between immune stimulation and suppression, and presumably, inhibition of PI3Kγ could facilitate the optimization of tumor immunity and improve patient prognosis.

To elucidate the effects on related pathways and cellular functionalities after PI3Kγ inhibition, KEGG pathway enrichment analysis indicated that it would exert obvious influences on B cell receptor and NF-κB signaling pathways (Fig. 1I). Then, within GO functional enrichment, PI3Kγ was involved in positive regulation of T cell activation, inflammatory response, and immune system process in biological processes (BP), participated in the composition of cell membranes in cellular components (CC), and was associated with hydrolase activity and chemokine sensitivity (Fig. 1J). Taken together, these results suggest that PI3Kγ could potentially be engaged in biological processes such as angiogenesis, T cell presentation, inflammation, and immunity by regulating the B cell receptor signaling pathway and the NF-κB signaling pathway.

3.2. Machine learning-based modeling to screen selective inhibitor skeletons against PI3K

The machine learning-driven process for screening PI3K inhibitors was depicted in Fig. 2A. First, 350255 structure−bioactivity pairs of compounds with inhibitory effects on PI3K four isoforms were retrieved from the GOSTAR database, aggregating the comprehensive and rigorously selected bioactivity data. The initial dataset underwent a rigorous cleaning process using the cheminformatics tool RDKit to guarantee high−quality data, which eliminated duplicate and incomplete entries, yielding a refined dataset of 179,224 structures, with their chemical and biological activity data sourced from 1633 relevant patents and literature in the GOSTAR database (Supporting Information Table S1). Subsequently, compounds were uniformly converted to ECFP4 expressions and categorized based on IC_{50} or K_i values, with those below 10 nmol/L defined as strong inhibitors, those beyond 10 nmol/L and below 1 μmol/L considered as weak inhibitors, and those beyond 1 μmol/L to undetectable considered as non-inhibitors (decoys). The chemical distribution status of the various PI3K inhibitors and the structural data distribution scenario based on the five properties are illustrated in Supporting Information Figs. S2 and S3. Following initial dimensionality reduction, the dataset was randomly partitioned into a training set for modeling and a test set for accuracy validation, maintaining a 3:1 ratio between the training and test sets. Randomly selected compounds from both the training and test sets were subjected to t-distributed Stochastic Neighbor Embedding (t-SNE), revealing the essential spatial overlap between them, thus guaranteeing the generalization of the model (Fig. 2B). Subsequently, to select the most suitable machine learning model for identifying PI3K subtype inhibitors, five algorithms—Baye, RF, SVM, NN, and FP-GNN—were selected for training. A comprehensive benchmarking of five computational models was conducted, evaluating performance metrics including precision, recall, F1-score, MCC, and accuracy. The assessment revealed that the RF algorithm demonstrated superior predictive capability for PI3Kγ inhibitor development, exhibiting marginal superiority over the deep learning-based FP-GNN architecture (Supporting Information Table S2). ROC curve analyses revealed that the RF model consistently achieved the highest AUC values in predicting inhibitors across all PI3K isoforms, substantiating its enhanced discriminatory capacity for delineating potent inhibitors from inactive compounds relative to comparator models (Fig. 2C, and Supporting Information Figs. S4−S7). The detailed analysis of the confusion matrix substantiated the best predictive performance of RF, rendering it ideal for the subsequent screening of selective inhibitor scaffolds (Fig. 2D and Supporting Information Fig. S8−S10).

The commercially available database, Topscience Database, with over 300,000 skeletons, was chosen for skeleton screening. Following data cleaning and processing, the predictive scoring of the RF model identified a series of scaffolds potentially inhibiting PI3Kγ, with the top three illustrated in Fig. 2E. Meanwhile, fragment analysis of PI3Kγ-specific inhibitors revealed that substituents like a benzene ring and an amino group appeared with high frequency (Fig. 2F and Supporting Information Figs. S11−S14). Thereafter, the indole skeleton with the highest score was chosen as the parent structure, using BROOD for fragment replacement to produce new compounds, with substituent fragments sourced from the ChEMBL31 database. SZMAP was instantly employed for visualization to analyze the effect of diverse substituents on the scaffold-target selectivity (Fig. 2G−J). The Color-Coded Solvent Polarity Guidance spectrum around the scaffold indicates water polarity preferences: Yellow regions recommend non-polar substituents; Purple regions suggest polar substituents. Compared to other isoforms, PI3Kγ exhibited unique water network distributions around the R1 and R2 substituent positions. Specifically, polar substituents at the R1 site could boost ligand stability through interactions with solvent water in the surrounding pocket. Conversely, non-polar substituents at the R2 site, such as benzene rings, can significantly increase the binding affinity for PI3Kγ, thereby improving the stability of the complexes.

3.3. Constructing a selective PI3K inhibitor IHA library with indole-based skeletons

In combination with ligand-receptor interaction and fragment docking analysis, potential PI3K inhibitors with indole as the fundamental skeleton were filtered, and an array of indole derivatives was designed and synthesized (Scheme 1). Starting with aniline **1**, the Sandmeyer reaction yielded oxime-based acetanilide intermediate **2**, which was further dehydrated and condensed under the condition of concentrated sulfuric acid and high temperature to generate intermediate **3**. Subsequently, the C-3 position in **3** underwent a condensation reaction with substituted aniline to produce the Schiff base analog **4a**. Upon further alkylation and acylation reactions were carried out on the N-1 position in **4a** to afford **5a−5f** and **6a−6e**, respectively. By replacing the

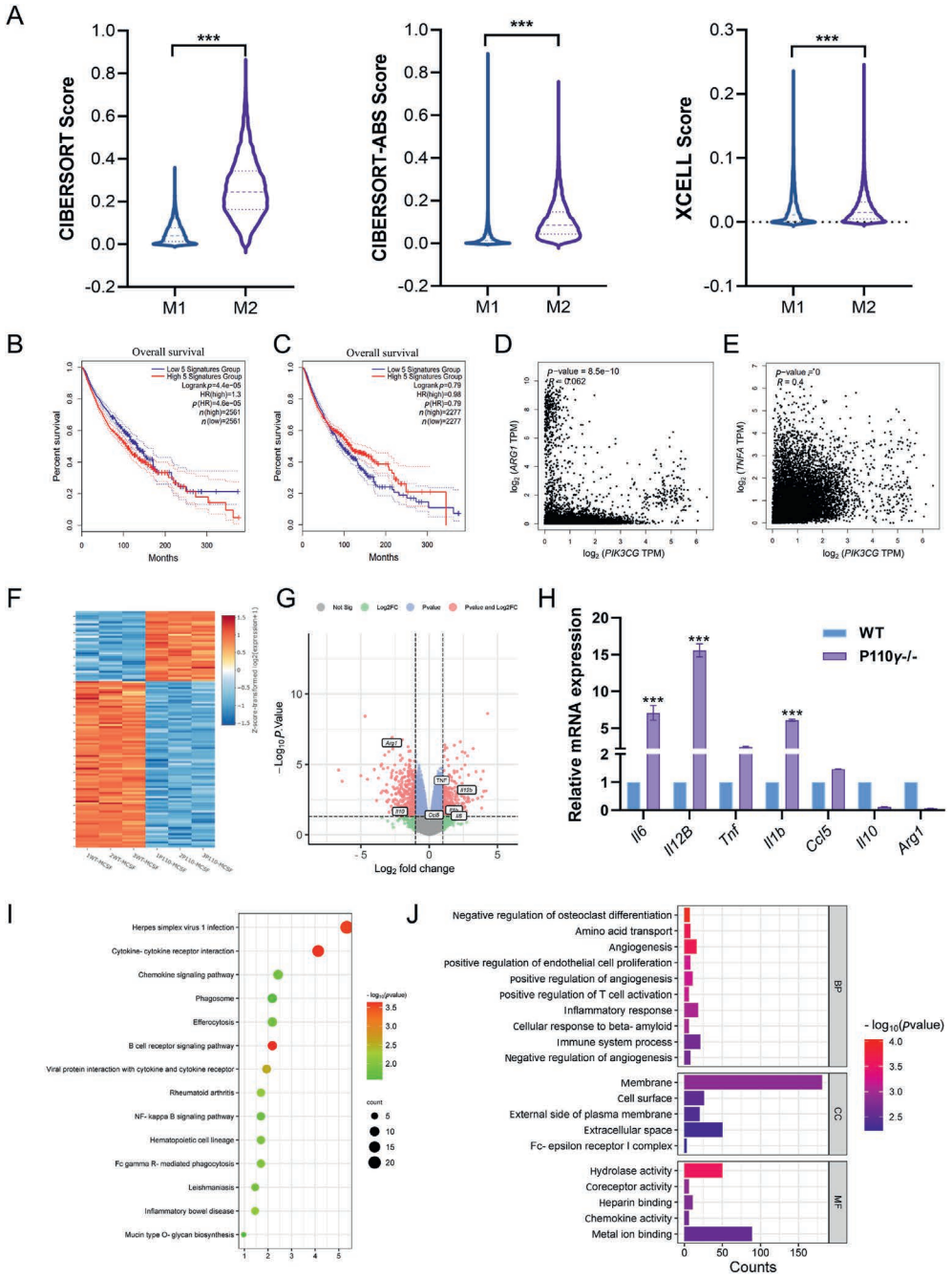

Figure 1 PI3Kγ in macrophage-mediated immune response to tumors. (A) CIBERSORT score, CIBERSORT-ABS score and XCELL score of TAMs (M1 and M2) in cancers. Data are shown as median ± interquartile range, $***P < 0.001$, Kruskal−Wallis test and Dunn's multiple comparisons test. (B) Kaplan−Meier survival analysis of TAM-M2 signature genes expression and the progression-free interval of cancer patients, log-rank test. (C) Kaplan−Meier survival analysis of TAM-M1 signature genes expression and the progression-free interval of cancer patients, log-rank test. (D) TAM-M2 signature gene (ARG1) associated with P110γ. (E) TAM-M1 signature gene (TNFA) associated with P110γ. (F) The mRNA expression heatmap in P110$\gamma^{-/-}$ *vs* WT macrophages ($n = 3$). (G) Volcano plot of differentially expressed mRNA in P110$\gamma^{-/-}$ *vs* WT peritoneal macrophages ($n = 3$). (H) TAMs associated mRNA expression in P110$\gamma^{-/-}$ *vs* WT peritoneal macrophages ($n = 3$), $***P < 0.001$, *vs* the WT group. (I) Top 15 KEGG pathways enriched by the differentially expressed proteins in P110$\gamma^{-/-}$ *vs* WT peritoneal macrophages. (J) GO analysis of the differentially expressed proteins in P110$\gamma^{-/-}$ *vs* WT peritoneal macrophages.

substituents, a series of compounds **7a−7j** was synthesized. Compounds **8a−8x** were prepared by substituting the N-1 position in **7a−7j** with different bromides under basic conditions. In the presence of sodium borohydride, the C═N bond in **8b** was selectively reduced to yield **9**. Unexpectedly, the substitution reaction with substituted benzylamines instead of substituted anilines afforded the rigid-structured bis-spirocyclic **10a−10e**. Subsequently, a carbene-catalyzed selective substitution reaction

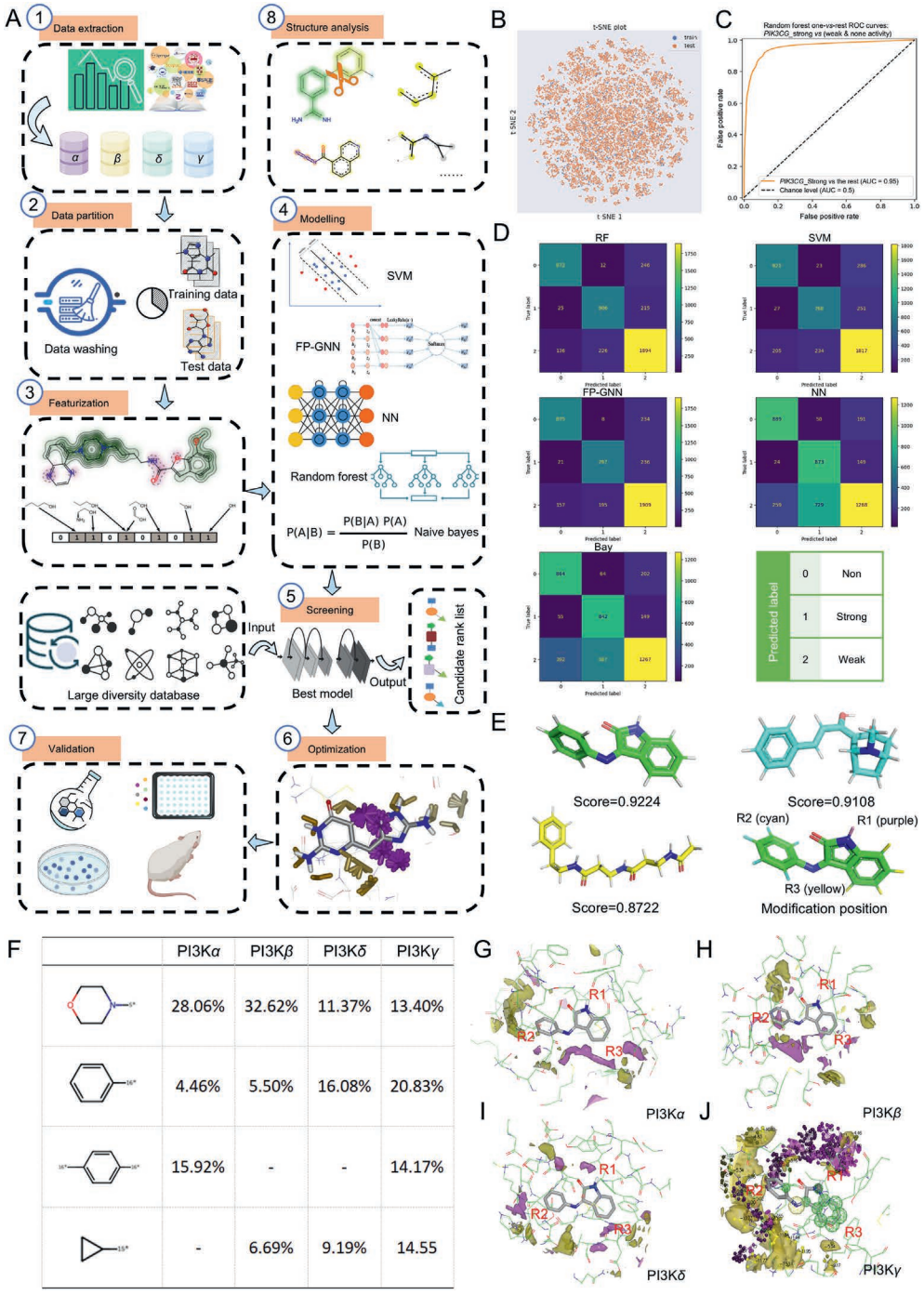

Figure 2 Machine learning-based screening for PI3K inhibitors. (A) Schematic diagram of the overall flow for the screening model. (B) Spatial dimensionality reduction of chemical features for training and test sets. (C) The ROC curve and AUC scores of RF models of PI3Kγ inhibitors. (D) The accuracy and confusion matrix of RF, SVM, Bay, NN, and FP-GNN models of PI3Kγ inhibitors. (E) The Reinforcement Learning algorithm screens for skeletons that selectively inhibit PI3Kγ. The yellow color represented modifiable positions in the skeleton. (F) Fragment analysis of PI3Kγ inhibitor-specific compounds. (G−J) SZMAP analyzed the polarity orientation of the scaffold in different subtype environments.

of **10** with unsaturated allyl aldehyde generated **11a−11d**, which were further derivatized to produce the lipid-soluble **12**. The chemical structures of all compounds were characterized by ^{1}H NMR and ^{13}C NMR (Supporting Information Fig. S15−S183). Consequently, the selective PI3K inhibitor compound library was established smoothly.

3.4. The IHAs with selective inhibition of PI3Kγ and antitumor activity

PI3K kinase suppression results indicated that all the synthesized compounds possessed favorable PI3K kinase inhibitory activity, with a 10- to 100-fold greater effect on PI3Kγ compared to other

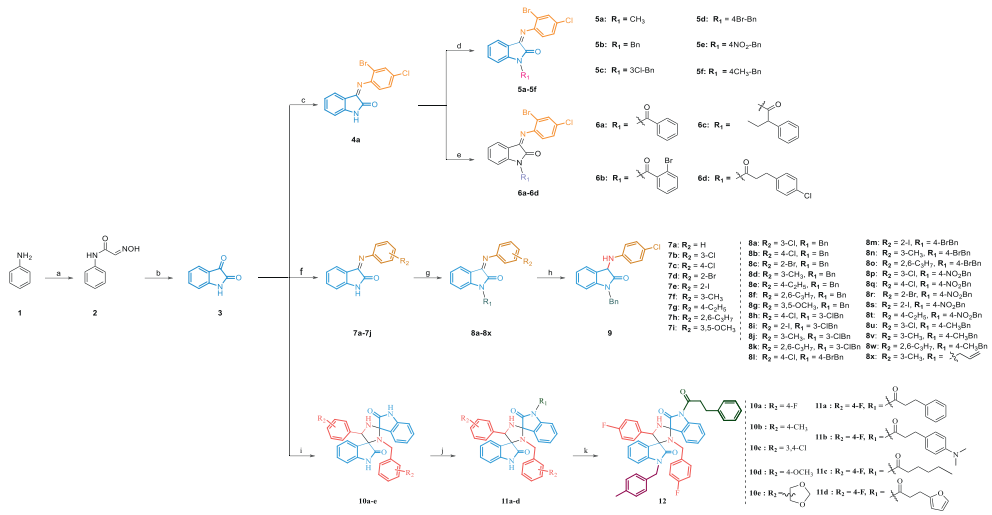

Scheme 1 Synthetic routes of IHAs. Reagents and conditions: (a) Aniline, Na_2SO_4, chloral hydrate, $NH_2OH \cdot HCl$, H_2O, 85 °C, 3 h, 88%; (b) Concentrated sulfuric acid, 90 °C, 1 h, 75%; (c) 2-Bromo-4-chloroaniline, acetic acid, EtOH, 70 °C, 4 h, 89%; (d) CH_3I, Cs_2CO_3 or R1, Na_2CO_3, DMF, r.t., 3−5 h, 73−97%; (e) 2-(7-Azabenzotriazol-1-yl)-*N*,*N*,*N*′,*N*′-tetramethyluronium hexafluorophosphate (HATU), *N*,*N*-diisopropylethylamine (DIPEA), DMF, 30 °C, 6−8 h, 58%−68%. (f) Compounds **7a−7j** was synthesized by the route of c, 3−6 h, 72%−96%; (g) Substituent group-Benzyl bromide, K_2CO_3, CH_3CN, 60 °C, 3−6 h, 70%−95%; (h) $NaBH_4$, EtOH, DCM, 0 °C, 8 h, 61%. (i) Substituent group-Benzylamine, CH_3CO_2H, C_2H_5OH, 80 °C, 2−5 h, 70%−85%; (j) NHC, DBU, $CHCl_3$, 4 Å MS, N_2, 24 h, 44%−48%; (k) *p*-Methyl benzyl bromide, K_2CO_3, DMF, 60 °C, 7 h, 87%.

isoforms, indicating a distinctive selectivity for PI3Kγ inhibition (Fig. 3A and Supporting Information Table S3). Notably, **5f** displayed potent inhibitory activity and high selectivity towards PI3Kγ with an IC_{50} of 0.11 nmol/L, compared to IC_{50} of 8.67 nmol/L, 9.63 nmol/L, and 5.91 nmol/L for PI3Kα, PI3Kβ, and PI3Kδ, respectively. Meanwhile, IPI-549 exhibited an IC_{50} value of 13.23 nmol/L for PI3Kγ kinase, representing 200-fold higher inhibitory activity against other PI3K subtypes. Comprehensive analysis indicated that **5f** demonstrated superior inhibitory activity against PI3Kγ kinase compared to IPI-549, though its kinase selectivity slightly lagged behind that of IPI-549. Molecular docking revealed **5f** binding to PI3K residues with isoform-specific selectivity driven by conformational heterogeneity in binding sites (Fig. 3B). Subsequent 50 ns MD simulations confirmed system stability (Supporting Information Fig. S184). **5f** demonstrated preferential targeting of PI3Kγ (−26.98 kcal/mol), significantly exceeding other isoforms (Supporting Information Fig. S185). The most thermodynamically favorable interaction observed with PI3Kγ (−26.98 kcal/mol) corresponds to the strongest binding affinity, suggesting isoform-selective targeting of PI3Kγ by **5f**. Bioinformatics analysis of common cancers indicated that *PIK3CG*, which encodes PI3Kγ, is highly expressed in melanoma, moderately expressed in colon cancer, and lowly expressed in breast cancer (Fig. 3C). MTT assays demonstrated that compounds from the established IHA library exhibited significantly lower IC_{50} values for tumor cells than for normal LO2 cells, indicating their antitumor potentiality. This activity may be associated with PI3Kγ inhibition, evidenced by the most pronounced effects on melanoma cells B16 with high PI3Kγ expression, and the least on breast cancer cells MCF-7 with low PI3Kγ expression (Fig. 3D and Supporting Information Table S4). Inspiringly, **5f** possessed the superior antitumor activity among many compounds, with IC_{50} values of 0.26, 0.64, and 3.04 μmol/L against B16, HCT116, and MCF-7, respectively, making it promising for melanoma treatment.

Preliminary structure-activity relationship analysis showed that the overall antitumor efficacies of **5b−5f** obtained by introducing alkyl groups at the *N*-1 position in **4a** were superior, and the inclusion of electron-donating substituents on the benzene ring, **5f**, could further enhance the tumor-suppressing effects. The unexpectedly notable diminution of antitumor activity was observed on **6a−6e** derived from the aromatic acyl substitution of the benzyl group, implying that greater lipophilicity facilitated improved ligand-protein binding. Moreover, the antitumor activity of **7h−7i** with double-substituted benzene rings was superior overall to that of mono-substituted **7b−7g**. Additionally, the antitumor activity of **8w** obtained by incorporating an electron-withdrawing group was overall preferable to that of **7a−7i**, whereas the antitumor activity of **8x** with the introduction of an electron-donating group was obviously diminished. Compared to **8a**, the antitumor activity of **9** obtained after the reduction of the Schiff base was attenuated, presumably due to its decreased electron-withdrawing ability. Regrettably, the antitumor activity of spirocyclic compounds **10−12** was not potentiated by the enhanced rigid architecture.

Leveraging inhibitory activity data from our previously synthesized compounds against PI3K isoforms, we established a QSAR model to predict inhibitory potency towards the four PI3K subunits, utilizing five molecular descriptors (Fig. 3E, Supporting Information Table S5). Model validation demonstrated superior predictive capability for PI3Kγ inhibition ($r = 0.84$), outperforming predictions for the α, β, and δ isoforms (Supporting Information Fig. S186). Critical descriptor analysis revealed atomic information content (a_IC) and the logarithm of the octanol−water partition coefficient (*S*log*P*) as paramount determinants of bioactivity. Their pronounced weighting within the model underscores that molecular structural complexity and the

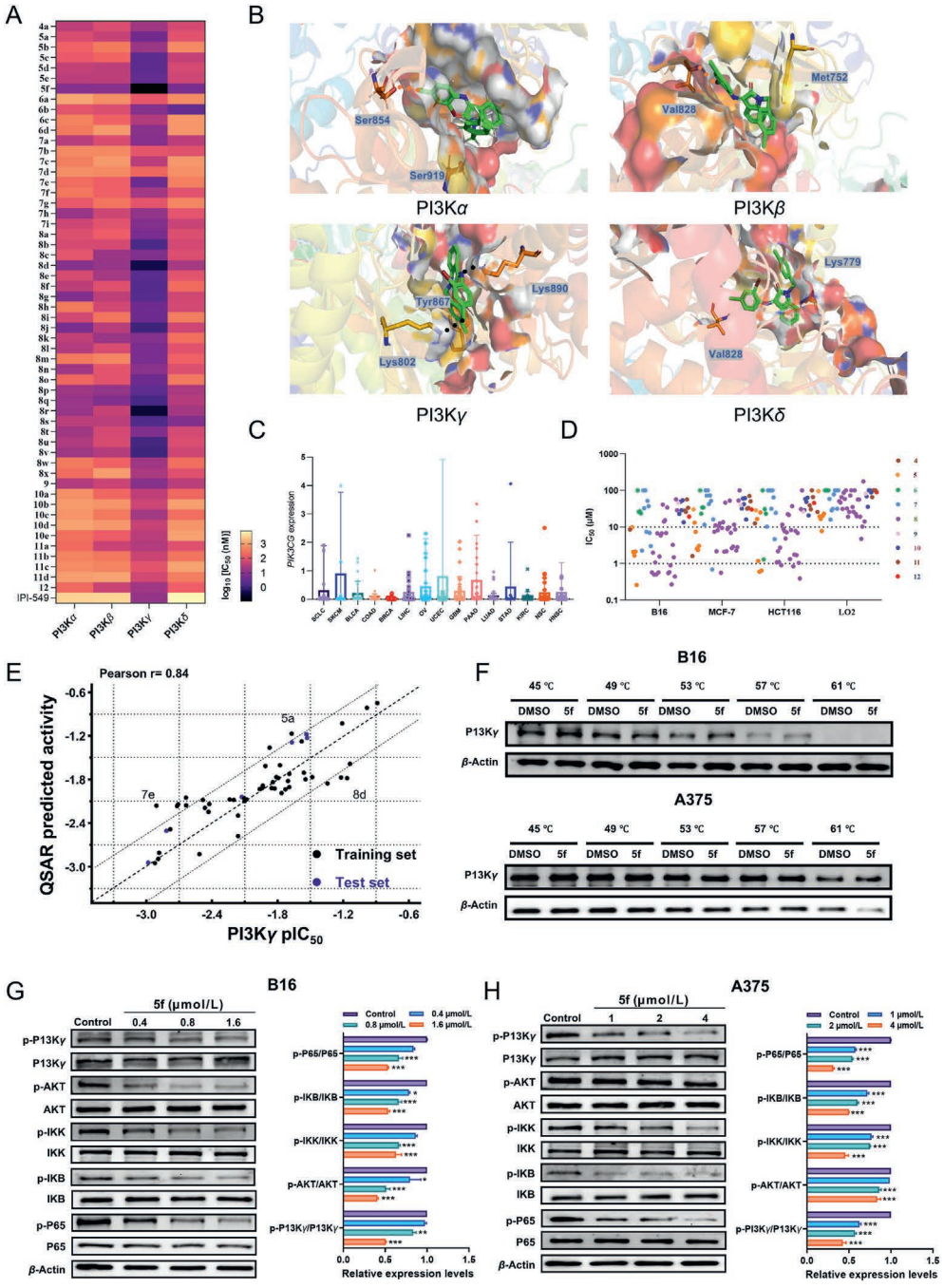

Figure 3 Selectivity of IHAs for PI3K enzymes and **5f** targeted binding to PI3Kγ. (A) Indole-based compounds towards the enzymatic activity for the four subunits of PI3K. (B) Differentiation of interactions between **5f** and PI3K subunits. (C) The expression levels of *PIK3CG* on different cancers. (D) The IC_{50} values of compounds on B16, MCF-7, and HCT116 cells. $IC_{50} > 50$ μmol/L uniformly was represented by 50 μmol/L. (E) The predictive ability of PI3Kγ QSAR models. (F) Western blot intensity of PI3Kγ in B16 and A375 cells treated with or without **5f** in the CETSA. (G, H) The PI3K/AKT/NF-κB pathway-related protein expression levels in B16 and A375 cells treated with **5f**, with β-Actin as a loading control. Data are expressed as mean ± SD, $n = 3$. $^{*}P < 0.05$, $^{***}P < 0.001$, *vs.* the control group.

lipophilicity−hydrophilicity balance constitute the principal physicochemical drivers governing selective inhibition across the PI3K isoforms. To elucidate the mechanistic basis for predicted selectivity, we conducted a visual analysis employing the *S*log*P* descriptor (Supporting Information Fig. S187). Computational mapping of the lipophilic potential across the binding pockets of all four isoforms delineated distinct site-specific preferences for ligand lipophilic/hydrophilic moieties. For instance, **5f** exhibited enhanced complementarity with the PI3Kγ pocket, where its hydrophilic chlorine, bromine, and oxygen atoms favorably engaged with hydrophilic regions of the binding site. The robustness in this model confirmed that these descriptors collectively captured the critical physicochemical drivers underpinning inhibitory potency and isoform selectivity.

3.5. PI3K/AKT/NF-κB pathway suppression of **5f** upon target-binding to PI3Kγ

The melanoma cell lines B16 and A375 were selected to investigate the binding of **5f** to PI3Kγ and its impact on associated signaling pathways. In comparison with the control group, the cellular thermal shift assay (CETSA) revealed that the **5f** administration elevated the thermal stability of PI3Kγ in melanoma cells, indicating the existence of a virtually direct interplay between **5f** and PI3Kγ (Fig. 3F). Subsequently, the molecular structure and pharmacophore calculations based on ROCS software revealed that **5f** comprised a variety of potential features such as aromatic rings, hydrogen bond acceptors, and hydrogen bond donors (Supporting Information Fig. S188A). In global structure mode, colorful ribbons and arrows characterized the PI3Kγ helix and chain, respectively, and the green stick pattern was assigned to **5f**, which was embedded in a protein pocket as observed (Fig. S188B). In the zoomed-in interaction illustration, **5f** was within a deep pocket and formed two hydrogen bonds with PI3Kγ protein residues (Fig. S188C). Specifically, the chlorine and nitrogen atoms in **5f** formed hydrogen bonds with Lys802 and Lys890 residues, respectively. Additionally, the two hydrogen atoms on the methyl group and the benzene ring produced aromatic ring-H interactions with Tyr867, respectively (Fig. S188D). PI3K/AKT/NF-κB, as an essential intracellular pathway, is intimately related to cell proliferation, apoptosis, and immunity. Western blot assays revealed that **5f** repressed the phosphorylation of PI3K/AKT/NF-κB pathway-related proteins, including p-PI3Kγ, p-AKT, p-IKK, p-IKB, and p-P65 in a dose-dependent manner (Fig. 3G and H). Meanwhile, the PI3K activator 740 Y-P abrogated the effect of **5f** on the phosphorylation of related proteins to a certain extent and reversed the **5f** inhibitory activity on the proliferation of B16 and A375 cell lines (Supporting Information Fig. S189A and S189B). Additionally, the antiproliferative effect of **5f** on B16 and A375 cells was significantly augmented by the co-administration of the PI3Kγ inhibitor IPI-549 (Fig. S189C and S189D). Specifically, **5f** displayed a superscripted or synergistic relationship with IPI-549 at high concentrations, which was equally present in the suppression of phosphorylation of proteins associated with the PI3K/AKT/NF-κB pathway.

3.6. The antiproliferative effect of **5f** on melanoma

An MTT assay was adopted to examine the proliferation inhibitory potential of **5f** on melanoma cells, revealing that **5f** apparently suppressed the B16 and A375 cell proliferation in a dose- and time-dependent manner, with IC_{50} values of 0.26 μmol/L and 0.97 μmol/L, respectively, for 48 h (Fig. 4A and B). Simultaneously, the viability of normal renal cells, HEK293 cells, was not impaired by **5f** at a concentration of 1 μmol/L (Fig. 4C). With increasing concentration of the administered **5f**, melanoma cells gradually underwent cell swelling, obviously visible cytoplasmic reduction, and enlarged nucleoplasmic ratio (Fig. 4D). Particularly, a massive cell detachment, cell swelling to 4−8-fold compared to the blank control group, and cell membrane collapse were observed in the high concentration group, which was more evident in the B16 cells. Subsequently, colony formation assay similarly revealed that **5f** inhibited melanoma cell proliferation in a dose-dependent manner (Fig. 4E). Moreover, quantitative EdU assay exhibited that **5f** dramatically inhibited melanoma proliferation, with 60.80% and 48.08% proliferation inhibition of B16 and A375 at the concentrations of 0.4 μmol/L and 1.8 μmol/L, respectively (Fig. 4F and G). Additionally, the proliferation inhibitory effect of **5f** on B16 and A375 cells could be reversed by 740 Y-P and potentiated by IPI-549, implying that **5f** exerted an inhibitory effect on the melanoma cell proliferation through the restriction of PI3Kγ (Supporting Information Fig. S190A−S190C). Meanwhile, the S-phase proportion of B16 and A375 cells elevated markedly from 27.36% to 28.50% to 57.65% and 39.76%, respectively, after the administration of **5f** at high concentration, suggesting that **5f** arrested the cell cycle in the S-phase to suppress cell proliferation (Fig. 4H and I). Western blot analysis further confirmed that S-phase-associated proteins Cyclin A and CDK 2 were dramatically diminished by **5f** (Fig. 4J and K). Altogether, the above findings demonstrated that **5f** suppressed cell proliferation through cell cycle arrest in a concentration-dependent manner.

3.7. The pro-apoptotic and anti-migratory effects of **5f** on melanoma cells

PI3K could exert anti-apoptotic effects through signal transduction. Employing Annexin-FITC and PI staining assay, **5f** promoted apoptosis of B16 and A375 cells in a concentration-dependent manner, bringing the apoptosis rate to 30.89% and 45.00% at 0.8 μmol/L and 2.7 μmol/L, respectively, with mostly early apoptosis (Fig. 5A and B). Moreover, ROS, as key intracellular signaling molecules, are involved in the initiation and execution of apoptosis. ROS levels detected by DCFH-DA staining revealed that **5f** boosted ROS concentration in B16 and A375 cells, which was probably an element of promoting apoptosis (Fig. 5C and D). Additionally, the pro-apoptotic mechanism of PI3K is intimately related to mitochondrial apoptosis-related proteins, and phosphorylation of Bad by activating the downstream protein Akt by PI3K leads to the depolymerization of BAD and BCL-2, with free BCL-2 exerting an anti-apoptotic effect. Through Western blot assay, **5f** was detected to facilitate the up-regulation of the expression levels of BAX, CYT C and cleaved CASPASE-3/8/9 in combination with the down-regulation of the expression levels of BID, BCL-2, PARP and CASPASE-3/8/9, implying that **5f** further initiated the mitochondrial apoptotic pathway through PI3K suppression to potentiate melanoma cell apoptosis (Fig. 5E and F). In the wound healing and Transwell migration assays, the cell migration capability after **5f** administration was obviously diminished, and the migration rate presented an inverse dependence on the **5f** concentration (Fig. 5G−J). Furthermore, against melanoma cells, 740 Y-P reversed the pro-apoptotic and migration inhibitory effects of **5f**, whereas coadministration of the PI3Kγ inhibitor IPI-549 augmented the apoptotic response (Fig. S190D−S190F). Overall, the above studies demonstrated that **5f** potently evoked melanoma cell apoptosis and repressed melanoma cell migration in a concentration-dependent manner.

3.8. The M2 polarization repression and M1 polarization promotion of TAMs by **5f**

PI3Kγ is a pivotal molecule in macrophage polarization with an intimate association with immunity, and its selective suppression enables the activation of NF-κB-related signaling, which favorably regulates the polarization phenotype of TAMs. Through

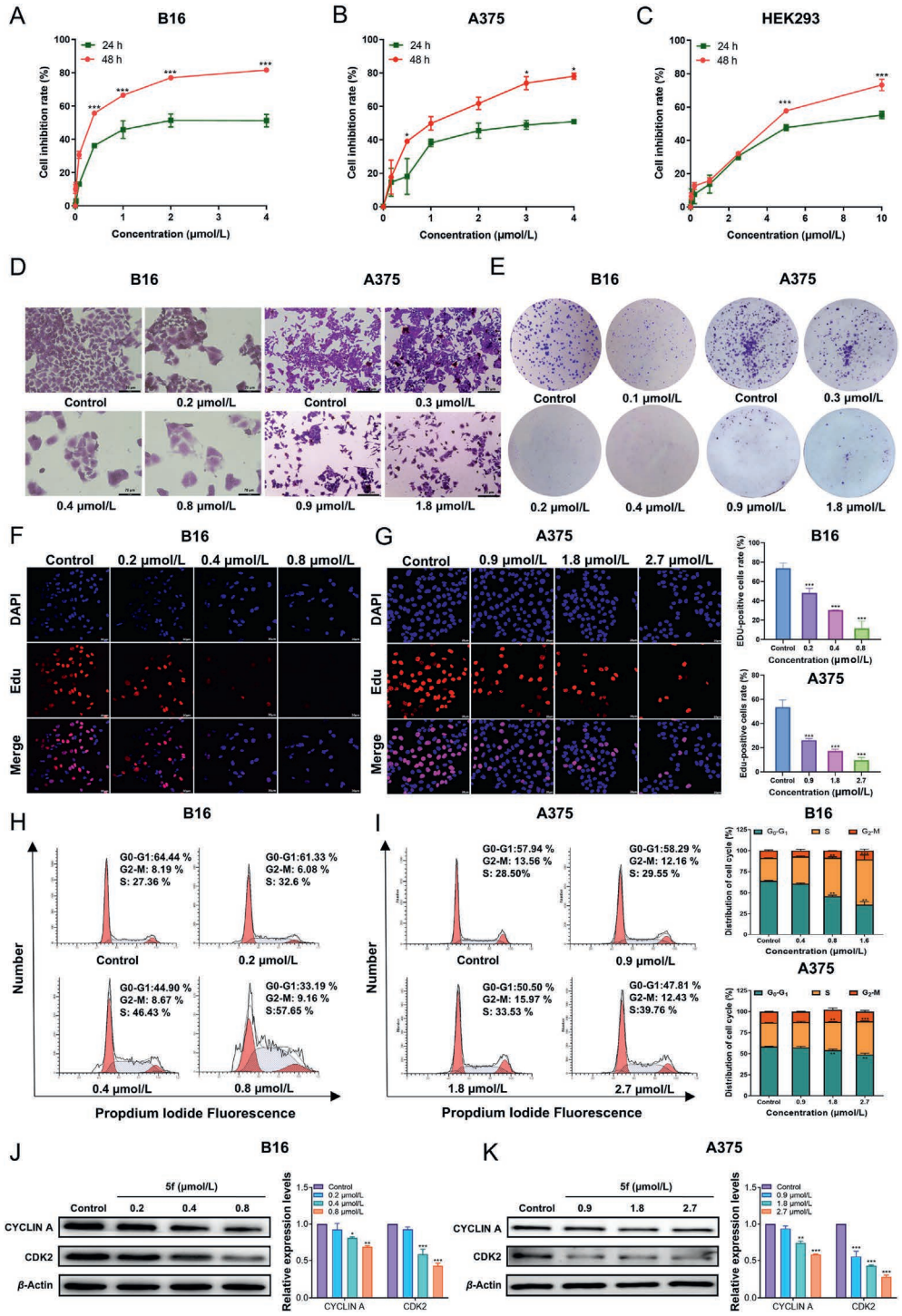

Figure 4 Effects of **5f** on proliferation and cycle arrest in B16 and A375 cells. (A−C) The cell inhibition rates of **5f** on B16, A375, and HEK293 cells by MTT. (D) The morphological changes of B16 and A375 cells after **5f** treatment, scale bar = 70 μm. (E) The effect of colony formation capability of **5f**-treated B16 and A375 cells after 48 h treatment. (F, G) Representative images of EdU-labeled B16 and A375 cells treated with **5f**, scale bar = 30 μm. Red: EdU, Blue: DAPI. (H, I) Cell cycle distribution of A375 and B16 cells was measured after **5f** treatment. (J, K) Western blot analysis of cycle-related proteins in B16 and A375 cells after **5f** treatment, with β-Actin as a loading control. The protein levels were normalized to the control group. Data are expressed as mean ± SD, $n = 3$. $^{*}P < 0.05$, $^{**}P < 0.01$, $^{***}P < 0.001$, *vs*. the control group.

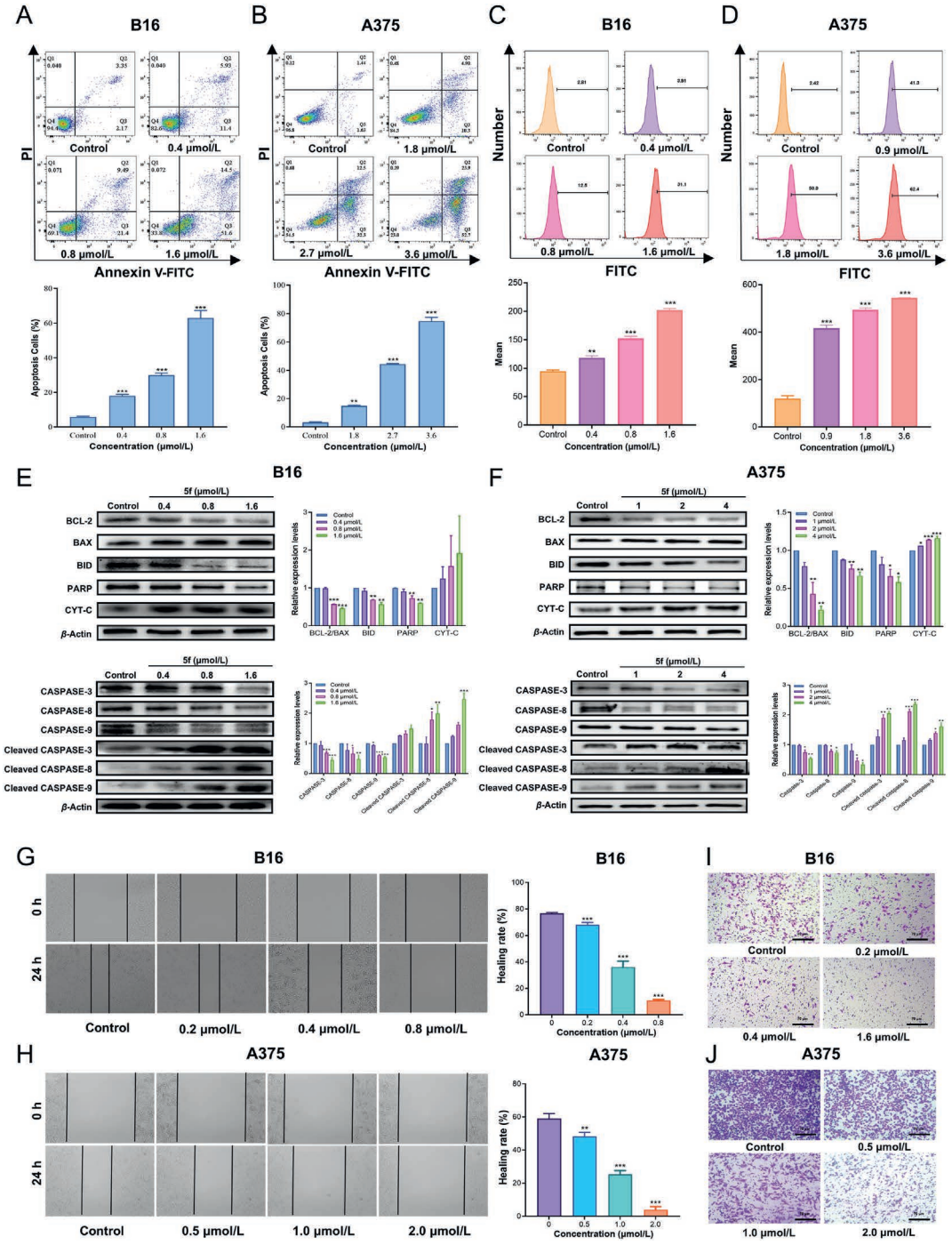

Figure 5 **5f** facilitated the apoptosis and suppressed the migration in melanoma cells. (A, B) Annexin V-FITC/PI staining was utilized to evaluate the apoptosis in B16 and A375 cells after **5f** treatment for 48 h. (C, D) The ROS generation in B16 and A375 cells treated with **5f**. (E, F) Western blot analysis for the apoptosis-related protein expression in **5f** treated B16 and A375 cells, with β-Actin as a loading control. The protein levels were normalized to the control group. (G, H) The effect of **5f** on the migration ability in B16 and A375 cells by wound healing assay. (I, J) The migration of A375 and B16 cells treated with **5f** was determined by Transwell assay, scale bar = 70 μm. Data are expressed as mean ± SD, $n = 3$. $^{*}P < 0.05$, $^{**}P < 0.01$, $^{***}P < 0.001$, *vs.* the control group.

confirming the impact of **5f** on mouse macrophage Raw 264.7, the cell viability was observed to be unaffected by concentrations below 5 μmol/L (Fig. 6A). Subsequently, the macrophages were conducted with non-toxic concentrations. To construct TAMs, a co-culture of B16 and Raw 264.7 cells was performed, and the cell phenotype was detected for further tracking (Fig. 6B and C). By detecting the expression of TAM-M1 marker CD86 and TAM-M2 marker CD206 under various treatment conditions, **5f** was indicated to repress IL-4 and IL-13-induced M2 polarization, with the proportion of M2 polarization diminishing from 36.90% to 10.30% at a concentration of 1.5 μmol/L (Fig. 6D). For TAMs constructed in cell co-culture, 84.8% of cells expressed CD206 as

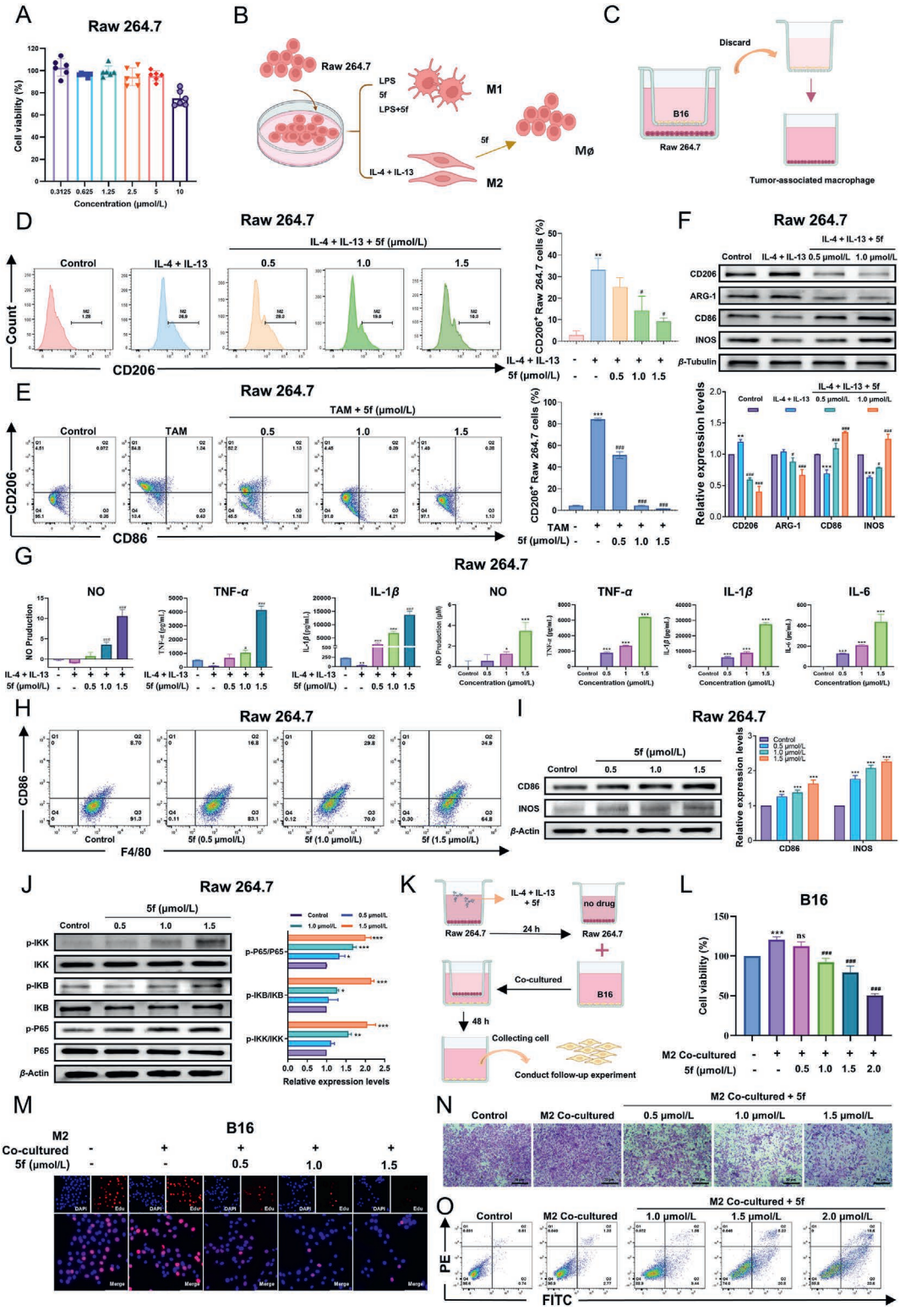

Figure 6 **5f** repressed M2 macrophage polarization and promoted M1 macrophage polarization *in vitro*. (A) Cell viability of Raw 264.7 cells after **5f** treatment *via* MTT assay. (B) Diagram of macrophage polarization. (C) Schematic diagram of constructing TAMs. (D) Flow cytometry analysis of CD206 expression in IL-4/IL-13 and **5f**-stimulated Raw 264.7 cells. (E) The expression of CD86 and CD206 in TAMs treated with **5f** *via* flow cytometry. (F) Western blot analysis for the expression levels of M1 (CD86 and INOS) or M2 (CD206 and ARG-1) polarization markers in RAW 264.7 cells after drugs treatment. (G) The M1-associated gene levels in the cell culture supernatants after **5f** combination with or without IL-4/IL-13 treatments. (H) The expression of CD86 and F4/80 in Raw 264.7 cells treated with **5f** was analyzed by flow cytometry. (I) Western blot analysis for the expression levels of M1 (CD86 and INOS) polarization markers in RAW 264.7 cells treated with **5f**. (J) Western blot analysis for the NF-κB signal-related proteins expression in Raw 264.7 cells treated with **5f**. All data are representative of three independent experiments. β-

polarized to M2-type macrophages. However, the proportion of CD206-positive cells dramatically declined in the presence of **5f**, decreasing to 1.4% at a concentration of 1.5 μmol/L (Fig. 6E). Moreover, evaluation of the expression levels of TAM-M2 markers (CD206 and ARG 1) and TAM-M1 markers (CD86 and INOS) by Western blot revealed that **5f** suppressed the expression of TAM-M2 markers and boosted the expression of TAM-M1 markers (Fig. 6F). Determination of TNF-α and IL-1β in culture supernatants of TAM-M2 by ELISA revealed that the levels of TNF-α and IL-1β were noticeably elevated by **5f** administration, as these normally raised their expression in TAM-M1 (Fig. 6G). The further related-factor detection uncovered that **5f** could enhance the contents of NO, IL-6, TNF-α, and IL-1β in Raw 264.7 culture supernatants (Fig. 6G). Additionally, the percentage of macrophage CD86 positivity with LPS alone was 39.1%, which increased to 88.9% when 1.5 μmol/L of **5f** was administered, and thus, **5f** in combination with LPS also exerted a remarkable effect on macrophage M1 polarization (Fig. 6H and Supporting Information Fig. S191). Western blot analysis of protein expression levels of TAM-M1 markers likewise demonstrated that **5f** promoted macrophage M1 polarization (Fig. 6I). Intuitively, from the morphological observation of Raw 264.7 cells, **5f** administration enabled the cells to gradually shift from round to sunflower shape, and for the macrophage morphology polarized toward M2, it showed an irregular long shuttle shape, which progressively transformed back to round shape after **5f** administration (Supporting Information Fig. S192). To further explore the mechanism by which **5f** promoted macrophage M1 polarization, an upregulation of the expression of p-IKK, p-IKB, and p-P65 was demonstrated to be boosted with **5f** (Fig. 6J). Overall, the above research suggested that **5f** suppressed macrophage polarization toward the M2 type and promoted macrophage polarization toward the M1 type by activating the NF-κB signaling pathway.

*3.9. The inhibitory effect of **5f** on M2-type macrophage-induced proliferation and migration of B16 cells*

An *in vivo* tumor-associated macrophage co-culture model was adopted to investigate the impact of **5f** on the proliferation and migration of B16 cells after repressing the polarization of M2-type macrophages. After **5f** administration for 48 h, M2-type macrophages were co-cultured with B16 cells in the Transwell chamber, and the co-cultured B16 cells were collected for relevant functional assays (Fig. 6K). B16 cell viability increased following co-culture with TAM-M2, which could be attenuated by **5f** administration in a concentration-dependent manner (Fig. 6L). The EdU assay results equally provided evidence in support of the above conclusions (Fig. 6M). Additionally, the migratory capability of B16 cells after co-culture with TAM-M2 improved, and the amount of cell migration increased dramatically, whereas the migratory capability of B16 cells declined considerably after co-culture with **5f**-treated M2-type macrophages (Fig. 6N). Moreover, the Annexin-FITC and PI double staining assay revealed that the apoptotic proportion of B16 cells increased from 4.1% to 44.2% after co-culture with **5f**-treated M2-type macrophages (Fig. 6O and Supporting Information Fig. S193). Collectively, in the *in vitro* co-culture system, **5f** evoked the transformation of M2-type macrophages to M1-type and repressed the melanoma B16 cells proliferation, migration, and promoted apoptosis.

*3.10. The in vivo antimelanoma potential of **5f** involving PI3Kγ-mediated TAMs-M2 polarization suppression*

The antimelanoma activity of **5f** *in viv*o was investigated using the B16-F10 transplanted tumor mouse model (Fig. 7A). Following 12 d of treatment, the tumors were stripped, weighed, and photographed for documentation. The results showed that **5f** possessed considerable antimelanoma activity, with the low-dose group (10 mg/kg) exhibiting activity comparable to the clinical drugs dacarbazine and IPI-549, while the high-dose group (20 mg/kg) achieved a tumor inhibition rate as high as 76.11% (Fig. 7B and C, and Fig. S194). Additionally, TUNEL staining revealed that administration of **5f** at 20 mg/kg significantly induced apoptosis, with effects equivalent to dacarbazine (Fig. 7D). H&E staining and Ki67 IHC staining revealed varying levels of cell necrosis and decreased proliferation marker staining across groups post-drug treatment, with the **5f** (20 mg/kg) group exhibiting the most pronounced effects (Fig. 7E). Besides, the **5f**-treated group showed no significant changes in body or major organ weights throughout the treatment, and no evident organ damage or abnormalities were observed; in contrast, the dacarbazine group exhibited a significant decrease in spleen weight, with minor blurring of the red and white pulp boundaries and cellular vacuolization in the spleen, as well as coagulative necrosis in the liver (Fig. 7F, and Supporting Information Fig. S195A and S195B).

Following the completion of treatment, TAMs in tumor tissue cell suspensions were identified with F4/80 and CD11B, and M2- and M1-polarized macrophages were characterized in TAM cell populations with CD206 and CD86, respectively (Supporting Information Fig. S196). As compared to the PBS control group, the percentage of M2 polarization in TAMs was diminished from 34.53% to 18.93% and 14.17% after treatment with 10 mg/kg and 20 mg/kg of **5f**, and to 15.40% after treatment with the positive drug, IPI-549, without meaningful distinction among the three groups (Fig. 7G and Supporting Information Fig. S197A). Similarly, immunofluorescence results revealed that both **5f** and IPI-549 could suppress the polarization of TAMs toward M2 and faintly facilitate M1 polarization (Fig. S197B and S197C). Furthermore, **5f** significantly suppressed p-PI3Kγ expression in tumor tissues *in vivo*, with less pronounced effects on p-IkKβ expression, possibly due to the intervention of alternative parameters in the complex *in vivo* environment (Fig. 7H).

5f exhibited no significant toxicity at therapeutic doses. To systematically evaluate its potential toxicological risks, escalating doses (100, 150, and 200 mg/kg) were administered for toxicity

Actin served as a loading control. The protein levels were normalized to the control group. (K) Schematic diagram of experimental design for co-culture assay with tumor and TAM-M2. (L) MTT assay detection of B16 cell *versus* bility after co-cultured with TAM-M2. (M) Representative images of EdU-labeled B16 co-cultured with TAM-M2, scale bar = 30 μm. Red: EdU, Blue: DAPI. (N) The migration of B16 cells co-cultured with TAM-M2 was determined by Transwell assay, scale bar = 30 μm (10 ×). (O) The apoptosis of B16 co-cultured with TAM-M2 was examined by staining with Annexin V/PI. Data are expressed as mean ± SD, $n = 3$. $^{*}P < 0.05$, $^{**}P < 0.01$, $^{***}P < 0.001$, compared to the control group. $^{\#}P < 0.05$, $^{\#\#}P < 0.01$, $^{\#\#\#}P < 0.001$, compared to the IL-4/IL-13 group or the M2 co-cultured group.

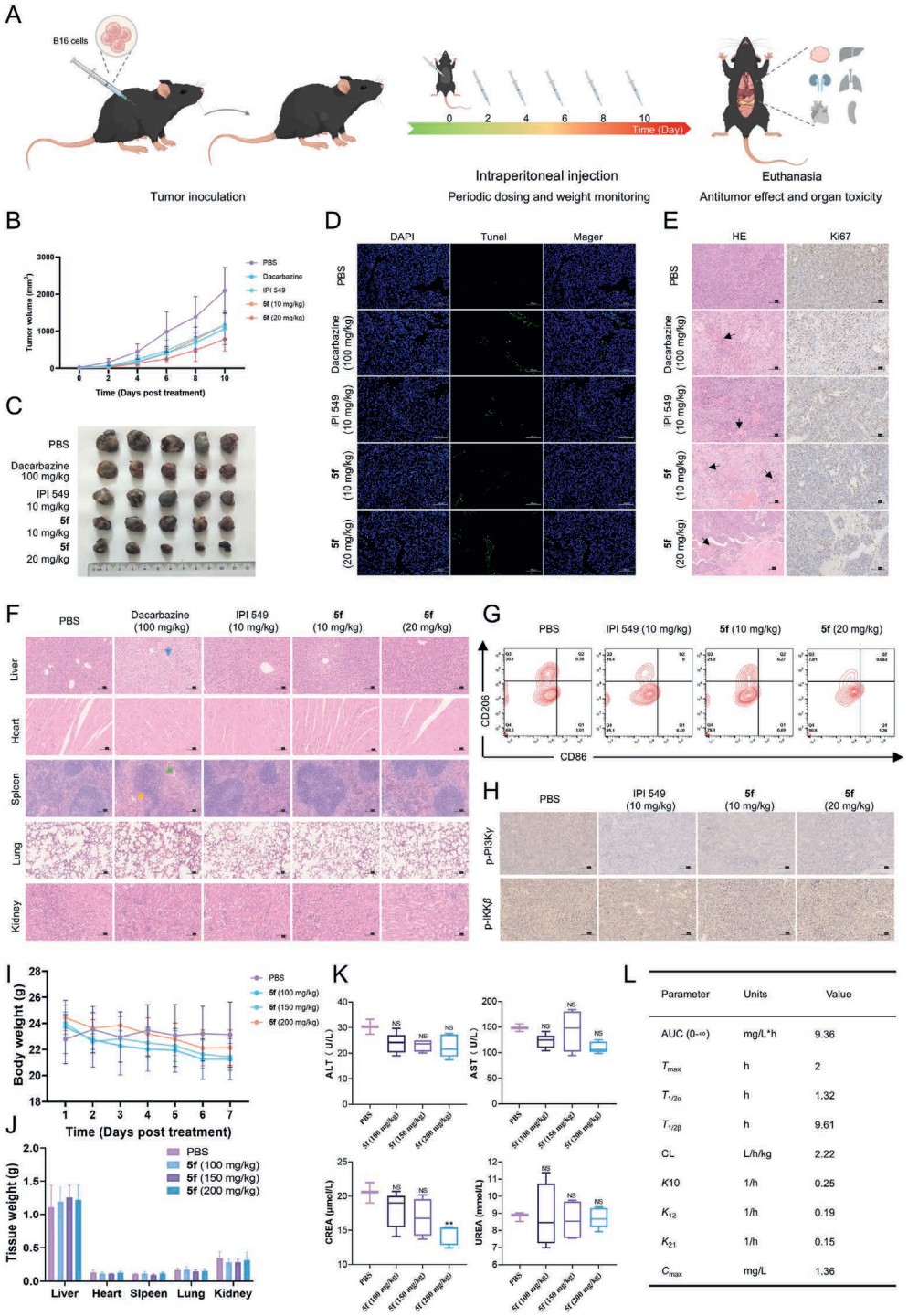

Figure 7 **5f** possessed therapeutic properties against melanoma in mice without noticeable toxicity by inhibited M2 macrophage polarization. (A) Schematic diagram of mouse tumor model construction and treatment protocol. (B) Tumor tissue growth curves in different treatment groups. (C) Pictures of the tumors extracted from mice on Day 10. (D) TUNEL staining of tumor sections, scale bar = 100 μm. (E) Representative H&E staining and Ki67 IHC staining images of tumor tissue, scale bar = 100 μm. The black arrows indicated the cell necrosis. (F) H&E staining images of major organs (heart, liver, spleen, lung, and kidney), scale bar = 100 μm. The blue arrow indicated the coagulative necrosis. The green arrow indicated the blurred demarcation between the white pulp and the surrounding red pulp, and the yellow arrow indicated the cell vacuolar degeneration. (G) The percentage of M1 macrophages and M2 macrophages was determined by flow cytometry. (H) Representative images of IHC staining of p-PI3Kγ and p-IKKβ in tumor tissues, scale bar = 100 μm. (I) Body weight changes during the treatment. (J) Tissue weight of heart, liver, spleen, lung, and kidney post-treatment. (K) Determination of ALT, AST, CREA, and UREA levels in mice serum from each treatment group. (L) Pharmacokinetic profiles of **5f** *in vivo*. ns, not significant, $^{*}P < 0.05$, $^{**}P < 0.01$, $^{***}P < 0.001$, compared to the PBS group.

assessment. Following 7-day consecutive treatment, all **5f**-treated groups manifested approximately 10% body weight reduction, suggesting incipient dose-dependent toxicity, though organ masses showed no statistically obvious alterations (Fig. 7I and J). Hematological parameters remained within normal physiological ranges (Supporting Information Table S6). Hepato-renal function analyses revealed no significant deviations in ALT, AST, or UREA levels at low-to-mid doses *versus* PBS controls (Fig. 7K). However, the 200 mg/kg group demonstrated markedly diminished UREA, indicating potential nephrotoxic propensity. Histopathological examination corroborated these findings: high-dose kidneys exhibited distinct renal tubular dilation and luminal enlargement, with sporadic mild splenic vacuolation observed (Supporting Information Fig. S198). Notwithstanding discernible nephrotoxicity at elevated doses, **5f** maintained a favorable therapeutic index. Subsequent pharmacokinetic investigations following intraperitoneal administration (20 mg/kg) yielded an elimination half-life (T1/2β) of 9.61 h (Fig. 7L, and Supporting Information Figs. S199 and S200). This protracted half-life signifies sustained plasma concentration stability, thereby ensuring continuous pharmacological efficacy while mitigating accumulation-mediated toxicological risks.

Taken together, **5f** exhibited pronounced antimelanoma effects *in vivo* without observable toxicity at therapeutic doses, demonstrating better safety than clinically used drug dacarbazine, and the antitumor effect of **5f** may involve PI3Kγ inhibition-mediated TAMs M2 polarization suppression.

4. Discussion and conclusions

TAMs constitute a key component of the tumor microenvironment, with their polarization into M1 and M2 phenotypes significantly influencing their functional outcomes. TAMs-M1 enhance antitumor immune responses through the secretion of pro-inflammatory cytokines and the activation of T cells. In contrast, TAMs-M2 contribute to tumor growth and metastasis by suppressing immune responses and promoting angiogenesis. Bioinformatics analysis revealed a significant correlation between PI3Kγ expression and M2-associated gene signatures in various cancers, highlighting a pivotal role of PI3Kγ in M2 polarization[30]. This was corroborated by our *in vivo* and *in vitro* experiments, suggesting that targeting PI3Kγ to modulate macrophage polarization represents a promising strategy in cancer immunotherapy.

The development of conventional PI3K inhibitors is constrained by the highly conserved ATP-binding domain across isoforms, resulting in insufficient selectivity and off-target toxicity. This lack of selectivity extends beyond PI3Ks to G protein-coupled receptor (GPCR) drug discovery, which faces analogous hurdles stemming from structural conservation. To overcome this, innovative strategies like genome-wide pan-GPCR cell libraries enable systematic screening for isoform-selective binders, a principle successfully applied in our discovery of **IHA-5f**[31,32]. In this study, a machine learning model (RF algorithm, ROC-AUC = 0.95) was employed to efficiently screen a library of >300,000 compounds, identifying a highly selective IHA scaffold. Subsequently, fragment replacement and molecular docking were utilized to evaluate the impact of substituents on ligand-target binding affinity and stability. This process was complemented by water-mediated pharmacophore optimization and MD simulations, enabling precise identification of key residues within the PI3Kγ-specific binding pocket, which led to the construction of an IHA compound library with potential selective PI3Kγ inhibitory activity.

Preliminary structure-activity relationship analysis through *in vitro* experiments revealed that nonpolar substituents, particularly those with high electron density, at the imine position (R2) of the IHA scaffold improved the binding stability of the small molecule. This resulted in high inhibitory activity and superior antitumor effects of the compounds, which aligned with the findings from computational simulations. Accordingly, a QSAR model was constructed to predict the inhibitory activity of compounds against PI3Kγ, yielding good predictive performance ($r = 0.81$). The representative compound, **5f**, exhibited picomolar inhibitory activity against PI3Kγ (IC_{50} = 0.11 nmol/L), addressing the lack of highly selective PI3Kγ inhibitors and demonstrating significant antitumor effects in various cancer cell lines, particularly in melanoma cells where PI3Kγ is highly expressed. Molecular docking revealed that the N atom in **5f** formed a hydrogen bond with the key residue Lys890 of PI3Kγ, achieving superior selectivity over other PI3K subtypes.

5f exerted synergistic anti-tumor effects through a dual mechanism: (1) direct tumor cell inhibition by targeting the PI3Kγ/AKT/NF-κB signaling axis, inducing S-phase arrest and mitochondria-dependent apoptosis in melanoma cells, as well as significantly suppressing migration; (2) immunomodulation by activating the NF-κB signaling pathway, reversing the M2 polarization of TAMs, promoting the release of pro-inflammatory cytokines (*e.g.*, TNF-α), and remodeling the immune-suppressive tumor microenvironment. This "two-pronged" approach overcomes the limitations of traditional PI3K inhibitors, which rely on a single-path approach, and provides a novel strategy for solid tumor therapy.

Currently, the development of PI3Kγ inhibitors is relatively scarce, with IPI-549 as a typical representative, which is commonly adopted in the treatment of hematological tumors and lymphomas[15]. In the B16-F10 tumor-bearing mouse model, **5f** (20 mg/kg) exhibited a tumor growth inhibition rate of 76.11%, significantly outperforming the clinical drug dacarbazine and the PI3Kγ-specific inhibitor IPI-549. Importantly, **5f** caused no organ dysfunction or weight loss ($P > 0.05$). Its exceptional safety profile stems from minimal cross-inhibition of PI3K$\alpha/\beta/\delta$, thereby avoiding the metabolic disorders and hematotoxicity commonly associated with pan-PI3K inhibitors[33,34]. Notably, **IHA-5f** demonstrated significant efficacy as a single agent, with a half-life of up to 9.61 h, whereas IPI-549 often requires combination with immune checkpoint inhibitors[35]. This highlights the potential of **5f** as a first-line antitumor agent, especially for melanoma treatment.

In conclusion, by leveraging machine learning with large-scale databases and employing molecular hybridization techniques, we have developed a series of PI3Kγ inhibitors featuring an IHA scaffold. Particularly noteworthy is representative compound **5f**, which exhibited picomolar potency in PI3Kγ inhibition and excellent antitumor activity, with its *in vivo* anti-melanoma effects superior to those of dacarbazine. This work highlights the potential of PI3Kγ inhibitors as immunomodulators that reshape the tumor microenvironment to facilitate cancer eradication, as well as their potential as direct antitumor agents.

Acknowledgments

This study was supported by the National Natural Science Foundation of China (82273812), the Sichuan Outstanding Youth Fund

Project (23NSFJQ0099 and 2023NSFSC1932, China), the Chengdu Science and Technology Bureau (2024-YF05-02599-SN, China), the Central Funds Guiding the Local Science and Technology Development of Sichuan Province (2024ZYD0090, China), the Sichuan Science and Technology Program (2024YFFK0172, China), the Guangdong Basic and Applied Basic Research Foundation (2024A1515030013, China), and the Shenzhen Commission of Science and Innovation programs (JCYJ20200109105613463, China).

Author contributions

Yi Zuo, Yiru Pu, Jianan Liu, and Hongyu Chen carried out the experiments and performed data analysis. Yao Chen, Yan Wang, Tingting Zhang participated part of the experiments and validated the data. Hongbin Cheng, Jin Liu, Zhaotong Cong contributed to the research design. Maolin Wang, Jun Lu, and Shilin Chen designed the research and supervised the project. All of the authors have read and approved the final manuscript.

Conflicts of interest

The authors have no conflicts of interest to declare.

Appendix A. Supporting information

Supporting Information to this article can be found online at https://doi.org/10.1016/j.apsb.2025.11.011.

References

1. Li XL, Liu R, Su X, Pan YS, Han XF, Shao CS, et al. Harnessing tumor-associated macrophages as aids for cancer immunotherapy. *Mol Cancer* 2019;**18**:177.
2. Gangadhara G, Dahl G, Bohnacker T, Rae R, Gunnarsson J, Blaho S, et al. A class of highly selective inhibitors bind to an active state of PI3Kγ. *Nat Chem Biol* 2019;**15**:348−57.
3. Yang HT, Wang YF, Liu W, He TP, Liao JY, Qian ZZ, et al. Genome-wide pan-GPCR cell libraries accelerate drug discovery. *Acta Pharm Sin B* 2024;**14**:4296−311.
4. Zhou SY, Liu ZC, Kawakami A. A PI3Kγ signal regulates macrophage recruitment to injured tissue for regenerative cell survival. *Dev Growth Differ* 2022;**64**:433−45.
5. Kaneda MM, Messer KS, Ralainirina N, Li H, Leem CJ, Gorjestani S, et al. PI3Kγ is a molecular switch that controls immune suppression. *Nature* 2016;**539**:437−42.
6. Postow M, Sullivan R, Cohen E, Gutierrez M, Hong D, Steuer C, et al. 434 updated clinical data from the melanoma expansion cohort of an ongoing Ph1/1b study of eganelisib (formerly IPI-549) in combination with nivolumab. *J Immunother Cancer* 2020;**8**. Available from: https://doi.org/10.1136/jitc-2020-SITC2020.0434.
7. Zhang ZZ, Richmond A. The role of PI3K inhibition in the treatment of breast cancer, alone or combined with immune checkpoint inhibitors. *Front Mol Biosci* 2021;**8**:648663.
8. Han MG, Jang B-S, Kang MH, Na D, Kim IA. PI3Kγδ inhibitor plus radiation enhances the antitumour immune effect of PD-1 blockade in syngenic murine breast cancer and humanised patient-derived xenograft model. *Eur J Cancer* 2021;**157**:450−63.
9. Isoyama S, Mori S, Sugiyama D, Kojima Y, Tada Y, Shitara K, et al. Cancer immunotherapy with PI3K and PD-1 dual-blockade *via* optimal modulation of T cell activation signal. *J Immunother Cancer* 2021;**9**:e002279.
10. Liu CQ, Cao YN, Zuo Y, Zhang CZ, Ren SM, Zhang X, et al. Hybridization-based discovery of novel quinazoline-2-indolinone derivatives as potent and selective PI3Kα inhibitors. *J Adv Res* 2025;**68**:459−75.
11. Castel P, Toska E, Engelman JA, Scaltriti M. The present and future of PI3K inhibitors for cancer therapy. *Nat Cancer* 2021;**2**:587−97.
12. Vanhaesebroeck B, Perry MW, Brown JR, André F, Okkenhaug K. PI3K inhibitors are finally coming of age. *Nat Rev Drug Discov* 2021;**20**:741−69.
13. Chen Y, Chen Y, Xu H, Liu JN, Wang Y, Zeng YJ, et al. GSH-responsive heterodimeric dual-targeted nanomedicine modulates EMT to conquer paclitaxel-induced invasive breast cancer metastasis. *Bioconjug Chem* 2025;**36**:1098−112.
14. Lanahan SM, Wymann MP, Lucas CL. The role of PI3Kγ in the immune system: new insights and translational implications. *Nat Rev Immunol* 2022;**22**:687−700.
15. Zhu JY, Li K, Yu L, Chen Y, Cai YF, Jin J, et al. Targeting phosphatidylinositol 3-kinase gamma (PI3Kγ): discovery and development of its selective inhibitors. *Med Res Rev* 2021;**41**:1599−621.
16. Al Hasan M, Sabirianov M, Redwine G, Goettsch K, Yang SX, Zhong HA. Binding and selectivity studies of phosphatidylinositol 3-kinase (PI3K) inhibitors. *J Mol Graph Model* 2023;**121**:108433.
17. Li K, Zhu JY, Xu L, Jin J. Rational design of novel phosphoinositide 3-Kinase Gamma (PI3Kγ) selective inhibitors: a computational investigation integrating 3D-QSAR, molecular docking and molecular dynamics simulation. *Chem Biodivers* 2019;**16**:e1900105.
18. Zhu JY, Ke K, Xu L, Jin J. Theoretical studies on the selectivity mechanisms of PI3Kδ inhibition with marketed idelalisib and its derivatives by 3D-QSAR, molecular docking, and molecular dynamics simulation. *J Mol Model* 2019;**25**:242.
19. Miles DH, Yan X, Thomas-Tran R, Fournier J, Sharif EU, Drew SL, et al. Discovery of potent and selective 7-azaindole isoindolinone-based PI3Kγ inhibitors. *ACS Med Chem Lett* 2020;**11**:2244−52.
20. Gu DY, Zhang MM, Li J, Zhou YB, Sheng R. Development of PI3Kγ selective inhibitors: the strategies and application. *Acta Pharmacol Sin* 2024;**45**:238−47.
21. Evans CA, Liu T, Lescarbeau A, Nair SJ, Grenier L, Pradeilles JA, et al. Discovery of a selective phosphoinositide-3-kinase (PI3K)-γ inhibitor (IPI-549) as an immuno-oncology clinical candidate. *ACS Med Chem Lett* 2016;**7**:862−7.
22. Chen Y, Yang JR, Wang CQ, Wang TB, Zeng YJ, Li X, et al. Aptamer-functionalized triptolide with release controllability as a promising targeted therapy against triple-negative breast cancer. *J Exp Cancer Res* 2024;**43**:207.
23. Zhang X, Chen Y, Li X, Xu H, Yang JR, Wang CQ, et al. Carrier-free self-assembled nanomedicine based on celastrol and galactose for targeting therapy of hepatocellular carcinoma *via* inducing ferroptosis. *Eur J Med Chem* 2024;**267**:116183.
24. Wang CQ, Xu H, Chen Y, Li X, Chen HY, Liu JN, et al. Hydroxyl-based acid-hypersensitive acetal ester bond: design, synthesis and the application potential in nanodrugs. *Eur J Med Chem* 2025;**283**:117153.
25. Kumar MR, Dhayabaran VV, Sudhapriya N, Manikandan A, Gideon DA, Annapoorani S. p-TSA center dot H_2O mediated one-pot, multi-component synthesis of isatin derived imidazoles as dual-purpose drugs against inflammation and cancer. *Bioorg Chem* 2020;**102**:104046.
26. Yin XM, Wang JY, Ge MH, Feng X, Zhang GG. Designing small molecule PI3Kγ inhibitors: a review of structure-based methods and computational approaches. *J Med Chem* 2024;**67**:10530−47.
27. Abraham MJ, Murtola T, Schulz R, Páll S, Smith JC, Hess B, et al. GROMACS: high performance molecular simulations through multi-level parallelism from laptops to supercomputers. *SoftwareX* 2015;**1**:19−25.
28. Valdés-Tresanco MS, Valdés-Tresanco ME, Valiente PA, Moreno E. gmx_MMPBSA: a new tool to perform end-state free energy calculations with GROMACS. *J Chem Theor Comput* 2021;**17**:6281−91.

29. Zeng YJ, Cao YN, Ren SM, Zhang CZ, Liu JN, Liu K, et al. Responsive ROS-augmented prodrug hybridization nanoassemblies for multidimensionally synergitic treatment of hepatocellular carcinoma in cascade assaults. *Adv Sci* 2025;**12**:e2501420.
30. Wang L, Wei C-Y, Xu YY, Deng XY, Wang Q, Ying JH, et al. Prognostic genes of melanoma identified by weighted gene co-expression network analysis and drug repositioning using a network-based method. *Oncol Lett* 2019;**18**:6066−78.
31. Chen W, Yu ZY, Leng L, Sun D, Liu H, Gong RZ, et al. Artificial intelligence-curated repository of gene-encoded natural diverse components from herbal medicines. *Innovation* 2025;**6**:101011.
32. Bi ZH, Li H, Liang YT, Sun D, Liu SX, Chen W, et al. Emerging paradigms for target discovery of traditional medicines: a genome-wide pan-GPCR perspective. *Innovation* 2025;**6**:100774.
33. Taylor EM, Byrum SD, Edmondson JL, Wardell CP, Griffin BG, Shalin SC, et al. Proteogenomic analysis of melanoma brain metastases from distinct anatomical sites identifies pathways of metastatic progression. *Acta Neuropathol Commun* 2020;**8**:157.
34. Gorlov I, Orlow I, Ringelberg C, Hernando E, Ernstoff MS, Cheng C, et al. Identification of gene expression levels in primary melanoma associated with clinically meaningful characteristics. *Melanoma Res* 2018;**28**:380−9.
35. Coma S, Weaver DT, Pachter JA. The dual PI3K-δ/PI3K-γ inhibitor duvelisib inhibits signaling and proliferation of solid tumor cells expressing PI3K-δ and/or PI3K-γ. *Cancer Res* 2020;**80**:663.